Petroleum Science 21 (2024) 1719–1738

Contents lists available at ScienceDirect

Petroleum Science

journal homepage: www.keaipublishing.com/en/journals/petroleum-science

Original Paper

The impact of heterogeneity and pore network characteristics on single and multi-phase fluid propagation in complex porous media: An X-ray computed tomography study

Shohreh Iraji [a, *], Tales Rodrigues De Almeida [b], Eddy Ruidiaz Munoz [c], Mateus Basso [d], Alexandre Campane Vidal [b]

[a] Department of Mechanical Engineering (FEM), State University of Campinas (UNICAMP), Campinas, SP, 13083-860, Brazil
[b] Department of Geology and Natural Resources, Geosciences Institute (IG), State University of Campinas (UNICAMP), Campinas, SP, 13083-855, Brazil
[c] LRAP/COPPE/COPPETEC/UFRJ, Rua Moniz Aragão 360, Bloco 4 Cidade Universitária, Rio de Janeiro, 21941-594, Brazil
[d] Center of Energy and Petroleum Studies (CEPETRO), State University of Campinas (UNICAMP), Campinas, SP, 13083-896, Brazil

ARTICLE INFO

Article history:
Received 3 May 2023
Received in revised form
29 December 2023
Accepted 17 January 2024
Available online 20 January 2024

Edited by Yan-Hua Sun

Keywords:
Pore network model
Heterogeneous porous media
Flow patterns
Dead-end pores

ABSTRACT

This study investigates the impact of pore network characteristics on fluid flow through complex and heterogeneous porous media, providing insights into the factors affecting fluid propagation in such systems. Specifically, high-resolution or micro X-ray computed tomography (CT) imaging techniques were utilized to examine outcrop stromatolite samples of the Lagoa Salgada, considered flow analogous to the Brazilian Pre-salt carbonate reservoirs. The petrophysical results comprised two distinct stromatolite depositional facies, the columnar and the fine-grained facies. By generating pore network model (PNM), the study quantified the relationship between key features of the porous system, including pore and throat radius, throat length, coordination number, shape factor, and pore volume. The study found that the less dense pore network of the columnar sample is typically characterized by larger pores and wider and longer throats but with a weaker connection of throats to pores. Both facies exhibited less variability in the radius of the pores and throats in comparison to throat length. Additionally, a series of core flooding experiments coupled with medical CT scanning was designed and conducted in the plug samples to assess flow propagation and saturation fields. The study revealed that the heterogeneity and presence of disconnected or dead-end pores significantly impacted the flow patterns and saturation. Two-phase flow patterns and oil saturation distribution reveal a preferential and heterogeneous displacement that mainly swept displaced fluid in some regions of plugs and bypassed it in others. The relation between saturation profiles, porosity profiles, and the number of fluid flow patterns for the samples was evident. Only for the columnar plug sample was the enhancement in recovery factor after shifting to lower salinity water injection (SB) observed.

1. Introduction

Comprehending the fluid flow through porous media is crucial for various industrial uses, including the recovery of hydrocarbons, underground water, and particle movement, CO_2 and hydrogen storage in subsurface reservoirs, flow through porous electrodes in fuel cells, and interstitial flow in biological tissues (Anbari et al., 2018; Raeini et al., 2014).

The total connected pores and pore geometry of rocks exert considerable control over the fluid flow within porous systems. Numerous studies using numerical simulations and two and three-dimensional image analysis show that the degree of connectivity and throat width are key factors in determining the characteristics and effective transport of porous rocks (Abedi et al., 2020; Doyen, 1988; Thomson et al., 2018; von Bargen and Waff, 1986; Wimert and Hier-Majumder, 2012). The coordination number, which is the total count of throats linked to a specific pore, is used to measure the level of connectivity within the pore network. These geometric characteristics of the pore network can vary depending

* Corresponding author.
E-mail addresses: shohre.iraji@gmail.com, siraji@unicamp.br (S. Iraji).

https://doi.org/10.1016/j.petsci.2024.01.015

on a number of variables; however, statistical studies of the structure, shape, size, and arrangement of porous systems enable determining these characteristics that are essential for the measurement of petrophysical properties (Rahmat et al., 2020; Thomson et al., 2018).

To explain the variability of pore network structure and textural alterations, conventional approaches to fundamental rock characteristic description fall short either in directly incorporating measurable geometric characteristics or in measuring the spatial distribution of the pores and grains in the three-dimensional network (Rezende et al., 2013; Thomson et al., 2018, 2020; Withers et al., 2021). X-ray computed tomography (CT) facilitates the assessment of these fundamental qualities and provides a more accurate direct visualization and characterization of the porous structure and geometry. This improves our comprehension of the pore volume and pore-network connectivity and microstructural constraints in various systems (Rezende et al., 2013; Thomson et al., 2018, 2020; Withers et al., 2021).

Properly describing the pore space is necessary for pore-scale modeling, especially when dealing with multi-phase flows (Al-Kharusi and Blunt, 2007). Pore-scale modeling of complex carbonate reservoirs is one of the scientific frontiers associated with the Brazilian Pre-salt play. The discovery of these reservoirs has been regarded as a significant breakthrough of the past decade and the cornerstone of South America's offshore petroleum industry. The main reservoir of the pre-salt play comprises unusual *in-situ* carbonate rocks formed by shrub-like and spherulitic calcite fabrics that were accumulated in extensional basins (Bruhn et al., 2017). These formations have complex geometries and diverse pore network structures. The growth framework, diagenetic modification, and depositional textures influence petrophysical properties based on rock features and control the pore volume and pores-throats connectivity (Lucia, 1983; Matula, 1969; Sharma, 2008). Different carbonate formations have been proposed as flow analogue rocks for the pre-salt reservoirs, including travertines (Claes et al., 2017) and microbialites such as stromatolites and thrombolites (Rezende et al., 2013).

In contrast to sandstone reservoirs, carbonate formations pose significant challenges in accurately determining petrophysical properties and characterizing reservoirs due to their high heterogeneity. Heterogeneity in reservoir description refers to the dispersion of parameters that impacts fluid flow (Hendry et al., 2021; Iraji et al., 2023a; Jensen et al., 2000; Sen et al., 2021). The heterogeneous nature and non-uniform distribution of petrophysical properties within carbonate formations give rise to significant ambiguity in constructing models and reasonably accurately forecasting production performance. Flow experiments allow for a precise evaluation of the influence of heterogeneity on fluid flow (Iraji et al., 2015; Iraji and Ayatollahi, 2019; Vik et al., 2013). Understanding the dynamics of fluid flow within the media and the behavior of various phases as they pass through the porous system is essential for enhancing reservoir recovery, predicting oil displacement efficiency and water injection performance, and overcoming the barriers that hinder oil retrieval through conventional recovery methods (Gunde et al., 2010).

The CT technique is a valuable tool for observing and quantifying fluid flow and variations in the liquid saturation field in porous media in 3D porous structures. This technique can display the spread and distribution of various fluids in porous materials and uncover the flow patterns of fluids using statistical computations (Su et al., 2022).

Heterogeneous stromatolite rock blocks collected from outcrops of Lagoa Salgada as the potential flow analogous of the Brazilian Pre-salt reservoir rock models (Wright and Tosca, 2016) were utilized in this study. Analysis of the geological features and pore geometry of these rock samples facilitated the identification of two distinct facies: fine-grained with smaller pores and less-connected pore networks and columnar (vugular) with a better-connected pore network and large vugs. Therefore, plugs were sampled considering these heterogeneities and facies. The first part of this study concentrated on providing a thorough account of the processing of the high-resolution or micro-CT images of the plug samples. The analysis employed digital rock physics (DRP) to evaluate and compare the pore network properties and geometry of fine-grained and columnar facies samples.

The second part of this article encompasses an extensive examination that merges traditional techniques such as core flooding with medical CT imaging to provide a characterization of porous systems, analyze single-phase and two-phase flow patterns during both drainage and imbibition processes, and explore the impact of varying salinity levels of injected water on oil flow. Moreover, using acquired CT images during flooding experiments, variations in the concentration profiles and saturation field were investigated during different flooding stages of water invasion and oil movement within the heterogeneous plug samples. The study aims to improve the understanding of the complex geometries and diverse networking patterns of the carbonate rocks, which have significant implications for hydrocarbon production and carbon and hydrogen storage in subsurface reservoirs of the Brazilian Pre-salt reservoirs.

2. Material and methodology

2.1. Materials

Outcrops of Lagoa Salgada in Rio de Janeiro State, Brazil, were used to perform experiments and evaluate the pore geometry and flow pattern. Fig. 1(a) displays the State of Rio de Janeiro, Brazil, highlighting the coastal zone and location map of the area of study. The geological characterization of the block rock sample was performed based on petrology and petrography to identify regions of interest and obtain representative rock facies before plugging samples. Two facies were specified: fine-grained and columnar/vugular (Fig. 1(b)). The first facies had relatively small pores, while the other had large pores and veins. In this work, one plug sample from columnar facies and two from fine-grained were drilled (Fig. 1(c)) to investigate and compare the effect of pore geometry on network characteristics, single-phase and two-phase flow patterns, saturation profile, and oil recovery. Since the plug samples were highly heterogeneous and frangible, the challenge was the preparation of a representative plug with constant marginal limits and maintained flow characteristics during fluid injection. A full description of the encapsulation techniques to overcome this challenge has been published previously published (Iraji et al., 2022a, 2022b, 2022c; Soltanmohammadi et al., 2021, 2022, 2024).

Porosity, gas permeability considering Klinkenberg correction, and physical properties of these plugs are listed in Table 1. For plugs from the columnar facies, given the existence of many linked pores and vugs, we could not calculate pressure drops during gas injection, and as a result, we could not measure gas permeability. So, liquid permeability calculation was conducted with three flow rates of 0.5, 1, and 5 mL/min using core flooding apparatus. The average liquid permeability of 5434.83 mD was determined using Darcy's law for the fluid flow in porous media for columnar plug.

The study used three different available aqueous solutions, namely distilled water (DW), sea brine (SB), and formation brine (FB). The compositions of FB and SB are displayed in Table 2.

The oil phase utilized in this investigation was obtained from the pre-salt reservoir. The oil was centrifuged and passed through a 5-μm Millipore filter before use. The oil properties and the results of SARA tests are presented in Table 3.

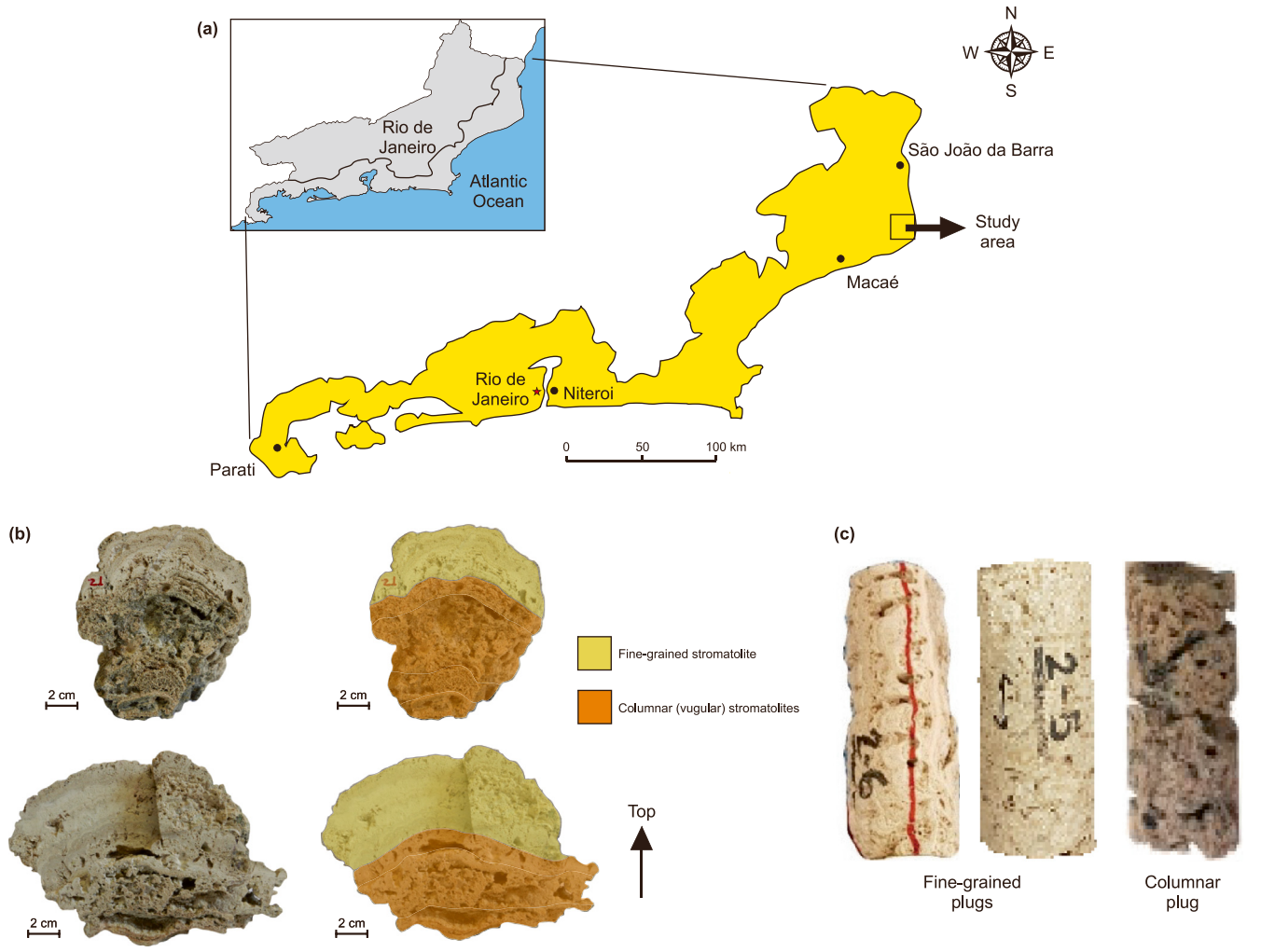

Fig. 1. (**a**) Coastal zone in Rio de Janeiro State with the marked location of the study area (Lagoa Salgada), (**b**) two main facies of rock sample, and (**c**) plug samples from the two facies.

Table 1
Petrophysical characteristics of the plugs.

Facies	Plug	Length, cm	Diameter, cm	Porosity, %	Gas permeability, mD
Fine-grained	F2-5	8.90	3.78	29.8	963
	F2-6	9.72	3.77	24.3	1200
Columnar	F1-1	8.90	3.68	52.4	–

Table 2
Average composition of SB and FB brine.

Brine	Composition, g/L									TDS, g/L
	NaCl	Na_2SO_4	$NaHCO_3$	KCl	$MgCl_2{\cdot}6H_2O$	$CaCl_2{\cdot}2H_2O$	$SrCl_2{\cdot}6H_2O$	$BaCl_2{\cdot}2H_2O$	$FeSO_4{\cdot}7H_2O$	
FB	163.62	0.088	0.487	6.911	3.068	19.100	0.029	0.033	0.022	193.358
SB	23.47	0.100	0.192	0.724	10.55	1.466	0.039	–	–	36.541

Table 3
Oil properties.

Parameter	Density, g/cm^3	Viscosity, cP	Molar mass, g/mol	Water content, %	Acid number, mg KOH/g oil	SARA composition, %			
						Saturates	Aromatics	Resins	Asphaltene
Value	0.8751	5	120	0.01	0.0275	93.26	0.59	5.82	0.33
Method	ASTM-D1298-12b, 2017	ASTM-D7042, 2014	ASTM-D2503-92, 1992	ASTM-D1744, 1992	ASTM-D664, 2011	ASTM-D6560-12, 2012			

2.2. Methodology

Fig. 2 displays an overview of the implemented workflow and this section offers a thorough clarification of each individual stage.

In the first step of the study, micro-CT image acquisition for both columnar and fine-grained plug samples was performed in the ZEISS Xradia Versa X-ray Microscopes, model XRM-500 (Voxel size of 44.69 μm) at the Laboratory of Porous Media and Thermophysical Properties of the Federal University of Santa Catarina (LMPT/UFSC). The image resolution (pixels) of each two-dimensional cross-sectional slice was 1029 × 999 with a slice thickness of 40 μm. These 2D micro-CT images were processed and stacked together to create the 3D representation of the plugs (Fig. 3). For determination and quantification of the porous phase of the plug samples, pore network modeling (PNM) was designed to gather information about the pore distribution, size and geometry of the pores and throats, and coordination number.

In the next step, core flooding experiments were designed and performed in the three plug samples to understand single-phase and two-phase flow propagation and saturation profiles with different pore geometry in the plug samples. The schematic of the core flooding experimental setup equipped with a medical CT scanner is shown in Fig. 4. The equipment consists of a horizontally held core holder, two high-pressure Quizix pumps for injection and confining pressure, liquid accumulators to transfer oil and brine, pressure and differential pressure transmitters, a back pressure regulator, a biphasic separator, the heating system, and a high precision data acquisition system connected to processing and controlling software. The medical imaging systems from SIEMENS, specifically the SOMATOM Spirit scanner (voxel size of 100 μm) at the Center for Energy and Petroleum Studies of the State University of Campinas (CEPETRO/UNICAMP), was utilized as a single source computed tomography device to acquire CT data of plug samples during the injection. The image resolution (pixels) was 512× 512 with a slice thickness of 0.1 cm.

This step-by-step procedure was followed for the flooding experiments (this process was applied to each of the three plugs).

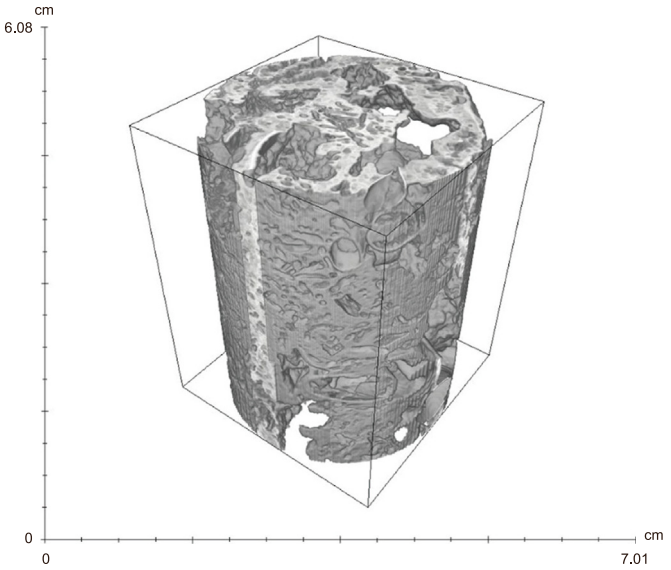

Fig. 3. 3D high-resolution full model of the columnar sample.

I. Assemble the dry plug sample into the core holder with respect to encapsulation techniques under the experiment conditions (106 °C temperature and 150 bar confining pressure).
II. Vacuum the plug to remove air from the void space.
III. Inject N_2 into the sample and increase the N_2 injection pressure step by step to the point that the pressure reaches 50 bar and then properly stabilizes.
IV. Perform CT scanning on the plug that has been saturated with N_2 (dry CT).
V. Vacuum the plug to remove N_2 from the void space.

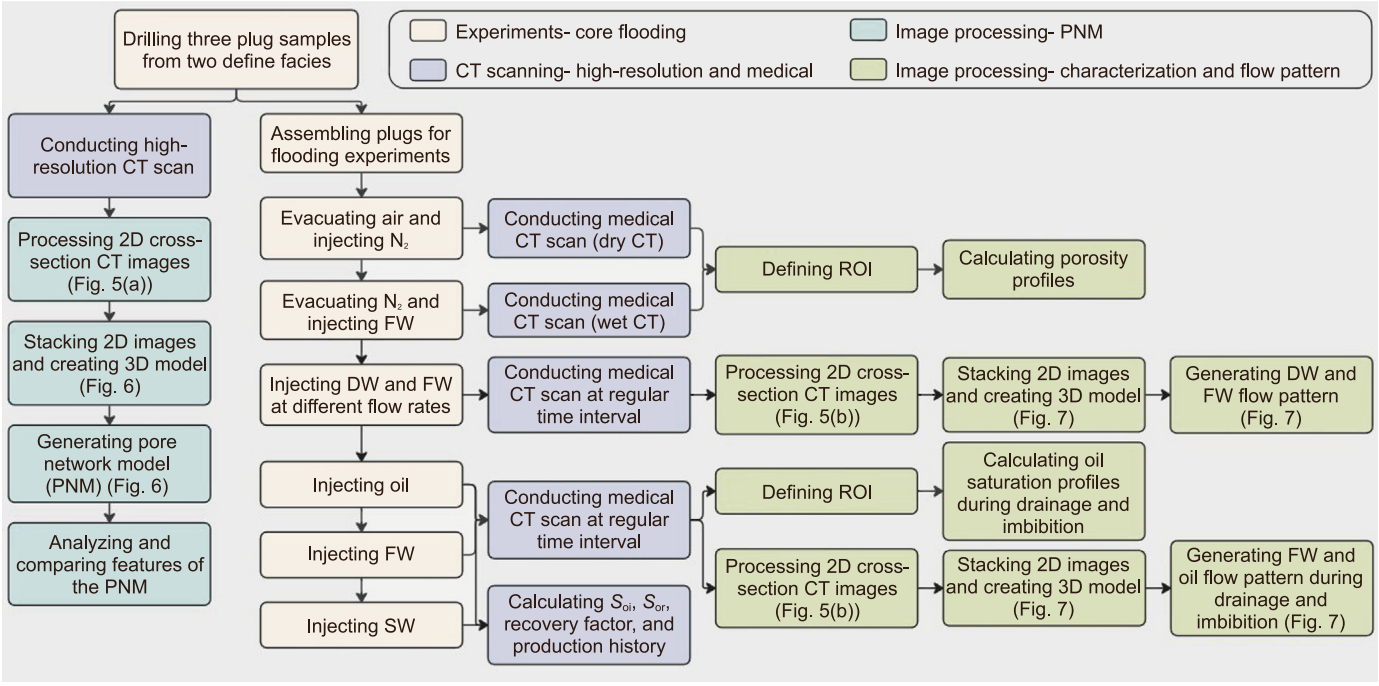

Fig. 2. Implemented workflow of the study.

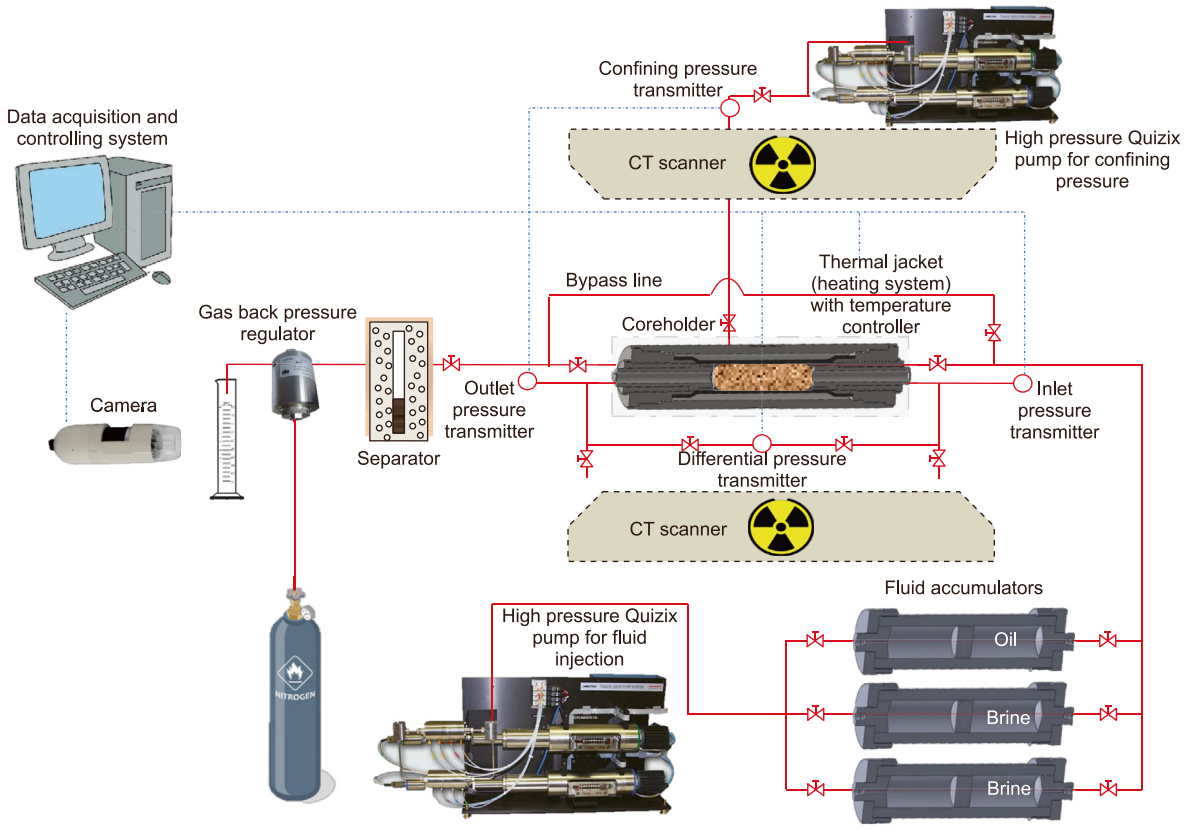

Fig. 4. A diagram of the experimental setup: core flooding equipment and the medical CT imaging system.

VI. Inject FB into the plug and continue the process until the pressure stabilizes (All the fluids were injected at experiment temperature).
VII. Perform CT scanning on the plug that has been saturated with FB (wet CT).

Note: Steps (III) to (VII) were performed to map out the porosity distribution and to obtain the initial description of the porous system.

VIII. Inject 2.0 pore volume (PV) of DW as the tracer with a consistent flow of 0.1 mL/min into the sample that has been saturated with FB and perform CT imaging while the process is ongoing.
IX. Inject 2.0 PV of FB with a consistent flow 0.5 mL/min combined with CT scanning during flooding.
X. Decrease flow rate to 0.1 mL/min and continue FB injection (several PV) until the total removal of the DW tracer.

Note: Steps (VIII) to (X) were performed to study single-phase and miscible process flow patterns.

XI. Inject 2.0 PV of oil with a flow of 0.1 mL/min into the sample that has been saturated with FB and acquire CT data during flooding.
XII. Inject 2.0 PV of FB at a flow rate of 0.1 mL/min combined with CT scanning during the injection. Record the production data, including pressure drop and produced volumes of oil and water, to calculate the recovery factor.

Note: Steps (XI) to (XII) were performed to study two-phase and immiscible process (drainage and imbibition) flow patterns and production of the saturation map during the injection process.

XIII. Inject SB at a constant rate of 0.1 mL/min. Continue SB injection until no further production of oil is observed. Keep track of the production data to measure the recovery factor and residual oil saturation.

Note: Step (XIII) was performed to find the efficiency of the ion change and lower salinity water injection on oil production.

It should be noted that, before starting oil injection (step XI) and after preparation of plug samples saturated with FB, some experiments were conducted by injection of FB at different flow rates (0.1, 0.5, and 1 mL/min for all three samples, for F1-1 vugular sample the higher rate of 5 mL/min was also applied to analyze flow regime and validate the application of the Darcy equation for these heterogeneous porous media with large pores and vugs. If the Darcy regime is dominant in our porous system, by plotting differential pressure over length versus velocity, we will have a straight line. Non-Darcy flow is indicated by a deviation from the straight line. This deviation demonstrates that, in non-Darcy flow, the pressure drop is greater than in viscous flow (Fetter, 2018).

2.2.1. Image processing

The X-ray is directed to the sample via various directions during CT imaging. The material is imaged in several 2D slices using the penetrating power of the X-rays (Lamas et al., 2019; Withers et al., 2021). Every X-ray beam with a single energy level attenuates differently as it passes the sample before being collected by a receiver. After measuring the attenuation from different angles, a

3D matrix is constructed. The attenuation numbers are reported in Hounsfield units (HU) at all points of the images (each array of the matrix) to show the variation of this parameter in the sample. The spatial distribution of the attenuation coefficient in rock samples is affected by differences in the level of empty space, types of minerals present, and degree of saturation (Hounsfield, 1973; Withers et al., 2021).

The current section describes the procedure of image processing. The dataset contains two sets of images for the plug samples, one with a high resolution (44.69 μm) and the other with a low resolution (100 μm). Medical CT scanning for acquiring low-resolution images was repeated during all steps of injection experiments for all samples.

Once the 2D CT data or sectional images have been obtained using the micro-CT scanner, the 3D model was generated by layering these images on top of each other in the Digital Rock Analysis software (PerGeos software version 2020.2), where the images were first binarized and segmented for the recognition and characterization of the porous system. To begin this process.

I. By cropping the images, a sub-area of the data was extracted to focus on a specific region of interest (Fig. 5(a)-Cropping).

The chosen sub-area diameters of 3.5 cm for micro-CT and 3 cm for medical-CT were selected based on careful considerations of the non-cylindrical nature of the plug samples (Fig. 1(c)). This decision ensures that each cross-sectional image exclusively captures the rock structure, accommodating plug sample diameter variations. The variation in diameter between micro-CT and medical-CT images arises from the distinct image acquisition conditions. Micro-CT images were obtained from scanned samples, while medical-CT images were acquired during core flooding experiments. A smaller diameter cut for medical-CT images was employed to mitigate the potential impacts of encapsulated material on analysis, maintaining the overall representation of the sample characteristics.

II. By applying a non-local means filter, the 8-bit grayscale CT images were treated to remove noise (Fig. 5(a)-Denoising).

Streaks, brightness nonuniformity, and phase shift edges at the rock grain borders are examples of these undesired artifacts and noises (Thomson et al., 2018).

III. Sharpening filters were implemented to the edges of the images to highlight the delimitation of the pore and rock edges (Fig. 5(a)-Sharpening) (Iassonov et al., 2009; Markussen et al., 2019).

IV. To partition the different compositional phases of the images (pores/grains separation), segmentation was enforced and a grayscale image was turned into a binary image according to the X-ray attenuation values of each voxel (Knackstedt et al., 2013). The interactive overlay threshold was applied to segment and binarize the images (Fig. 5(a)-Binarization).

V. A 3D model was created by arranging the segmented 2D images on top of one another. Fig. 6(a)–(d) displays 3D visualizations of the sample considering grains, total, isolated, and connected pore spaces.

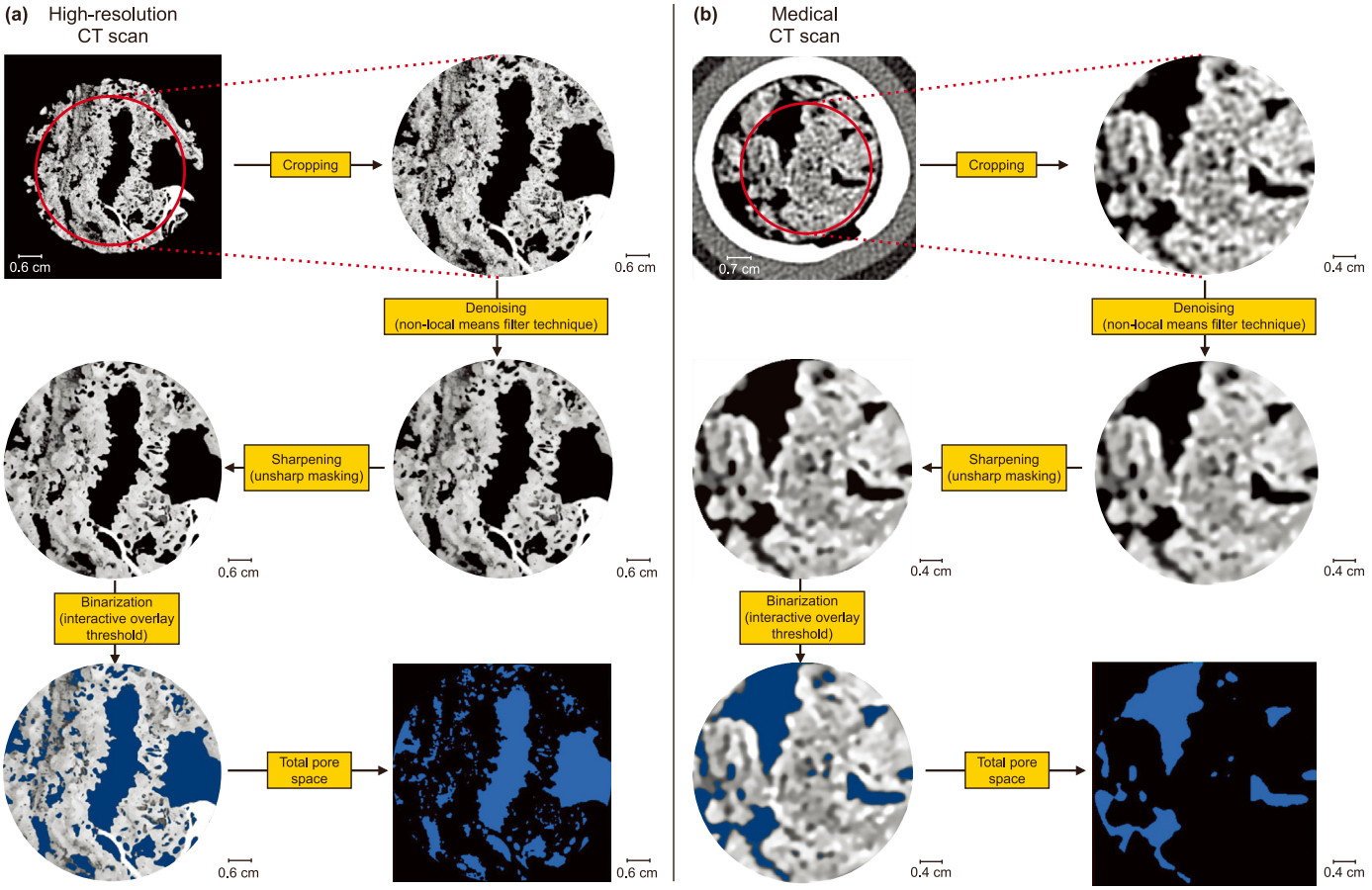

Fig. 5. Image processing procedure for (**a**) 2D micro-CT scan and (**b**) 2D medical CT scan.

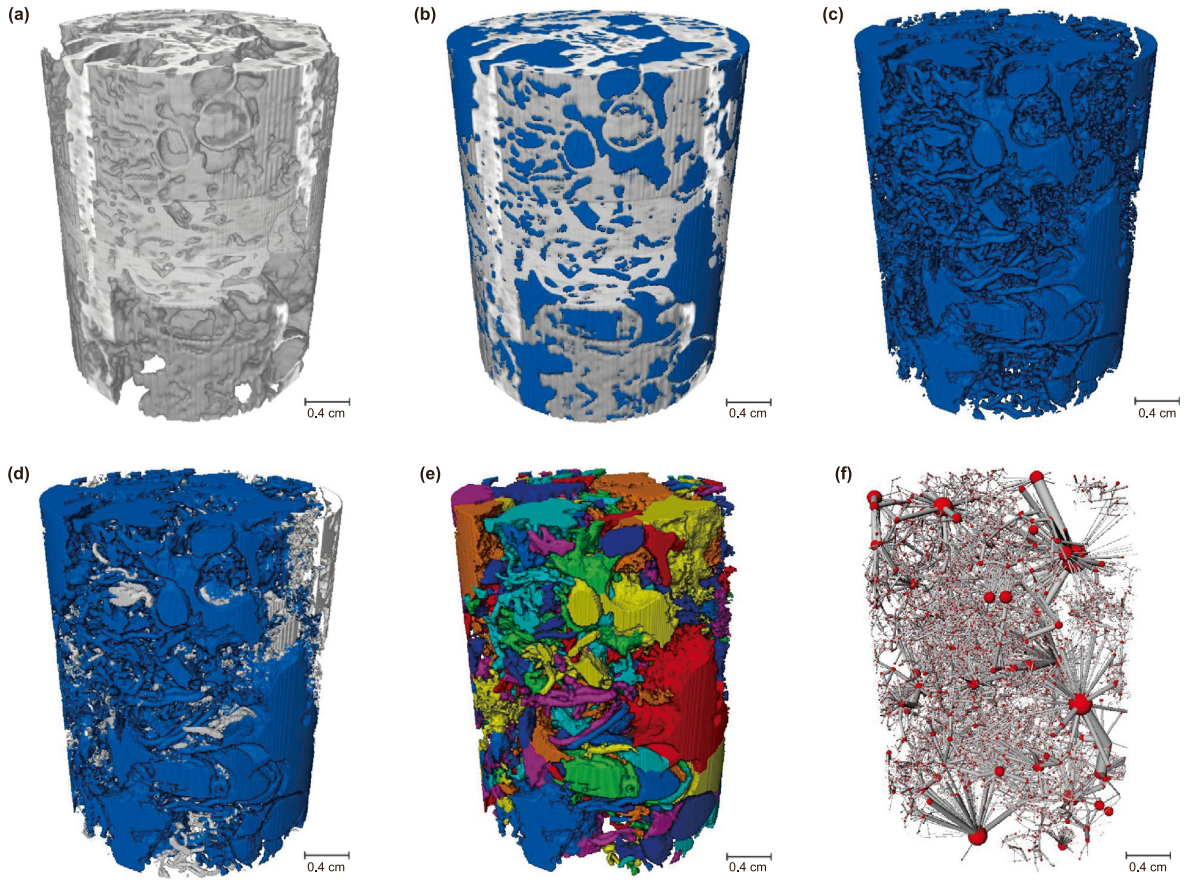

Fig. 6. 3D representation of sample obtained from micro-CT scan images for (**a**) grain (gray), (**b**) grain (gray) and total pores (blue), (**c**) total pores (blue), (**d**) connected pores (blue) and isolated pores (gray), (**e**) separated pore space, and (**f**) resulted pore network model.

VI. The pore network model (PNM) was generated using PNM module in PerGeos for further processing the 3D models and to evaluate the connection between the characteristics of porous structure, such as the radius of pore and throat, coordination number (the number of connecting throats attached to a specific pore), shape factor, and the volume of pores.

Pores and throats are the two main parts of the pore network, where grain corner pores serve as junctions between distributed linear throats along grains. PNM module utilizes the hybrid algorithm to make a framework of the total pore system. This is achieved by determining the minimum spatial separation of voxels in the foreground (empty region) and background, thus eroding the pore-grain interface and calculating the line length and connectivity. Lines with an outermost radius larger than their length are classified as pores, while those with a smaller radius are designated as throats. In the next step, the resulting image is resized to fill the border of every pore and throat, and the radius and length of each throat are calculated (Thomson et al., 2018, 2020). Fig. 6(e) displays the marked image which is the outcome of this procedure, with distinct pores and throats dyed in different hues, and Fig. 6(f) displays the resulted PNM.

Subsequently, the 2D images acquired from medical CT scanning during flooding experiments were processed. Steps (I) to (V) for binarization, segmentation, and generating 3D models were repeated and performed for all low-resolution images of plug samples (Fig. 5(b)). 3D representation of the sample for grains, total, isolated, and connected pore spaces for medical CT images are displayed in Fig. 7(a)–(d). Finally, to generate flow patterns, the binary image file of the porous system was used as a mask in the separation of fluids. The injected fluids (brine or oil) were segmented according to the watershed algorithm and according to the X-ray attenuation values of each fluid (Table 4). After this segmentation, the connectivity of the pores was investigated through the axis connectivity tool by analyzing the binary 3D image of all paths of each fluid in the porous system (PerGeos, 2019). If there is no connectivity between the fluid inside the pores, it may be necessary to perform a new segmentation process until connectivity is achieved. This means that the segmentation algorithm should be modified or refined to accurately identify and delineate the connected regions of the fluid within the pores. The goal is to ensure that the segmented regions represent physically connected areas of the fluid, allowing for meaningful analysis and interpretation of the porous media. Fig. 7(e) displays the results of the axis connectivity tool using oil attenuation value and reveals part of the connected pore space in which the oil flows. Moreover, Fig. 7(f) shows the resulting oil flow pattern during one flooding experiment.

Meanwhile, using the medical CT images obtained during flooding experiments, the average porosity was determined for each slice, which allowed for creating a porosity profile along the plug (according to dry and wet CT). As previously stated, medical CT imaging of the plugs was performed at each stage of the flooding experiment (every 0.2 PV fluid injection) to evaluate the arrangement of saturation level and indicate the fluid movement. The following equations were used to obtain porosity and oil saturation profiles during the drainage and imbibition.

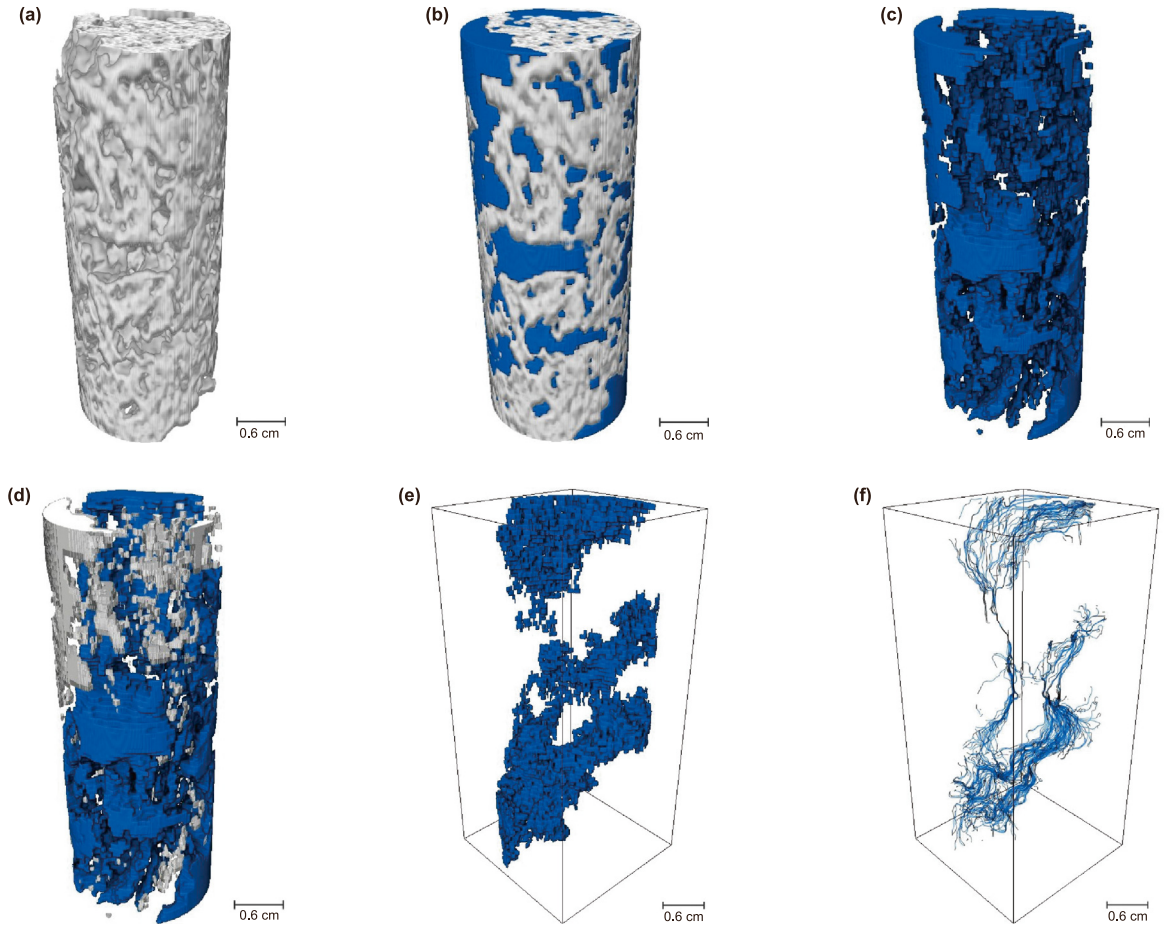

Fig. 7. 3D representation of sample obtained from medical CT scan images for (**a**) grain (gray), (**b**) grain (gray) and total pores (blue), (**c**) total pores (blue), (**d**) connected pores (blue) and isolated pores (gray), (**e**) connected pores filled with oil, and (**f**) oil flow pattern.

Table 4
The average CT attenuation data of the fluids at the experiment conditions.

Fluid	CT value (HU)
N_2	−545.52
FB	433.03
DW	389.17
Oil	29.68

$$\phi = \frac{CTR_w - CTR_g}{CT_w - CT_g} \quad (1)$$

$$S_o = \frac{CTR_w - CTR_{wo}}{\phi(CT_w - CT_o)} \quad (2)$$

where CTR_w, CTR_g, and CTR_{wo} represent the CT attenuation coefficient of the plug saturated with FB, saturated with N_2, and saturated with both oil and FB; CT_w, CT_g, and CT_o represent the mean CT attenuation coefficient of the FB, N_2, and oil under experimental pressure and temperature, respectively.

In more detail, for calculating porosity and saturation curves during experiments, a script written in the Python programming language was created specifically for the purpose of analyzing and manipulating 2D medical CT images. The first step of this process involves defining a region of interest (ROI) by including both grain and pore spaces of plugs and excluding the components located on the outer side (encapsulation materials, sleeve, core holder, and air). Additional information about this algorithm for non-cylindrical and vugular samples is available from elsewhere (Iraji et al., 2023b). In the next step, average CT values of the ROI for acquired images during different stage of experiments were utilized to calculate saturation and porosity profiles during the process (Eqs. (1) and (2)).

3. Results and discussion

3.1. Porosity and pore network modeling

3.1.1. Pore network characteristics from micro-CT images

Applying the PNM, the entire porous system was categorized as a system of pores and throats. Figs. 8 and 9 demonstrate the 3D visualization of the porous space structure and pore network model for the columnar and one fine-grained facies sample, respectively. The PNM illustrations (Figs. 8(c) and Fig. 9(c)) use gray cylinders to depict the throats and spheres representing pores. The columnar sample features fewer, broader throats connecting the pores and a less dense pore network, while a compact network of narrow throats makes up the model of the fine-grained sample.

Fig. 10 compares the probability distribution plots of the pore geometry properties for both facies. The plots demonstrate the distribution of coordination number (Fig. 10(a) and (b)), shape factor (Fig. 10(c)), throat length (Fig. 10(d)), pore radius (Fig. 10(e)),

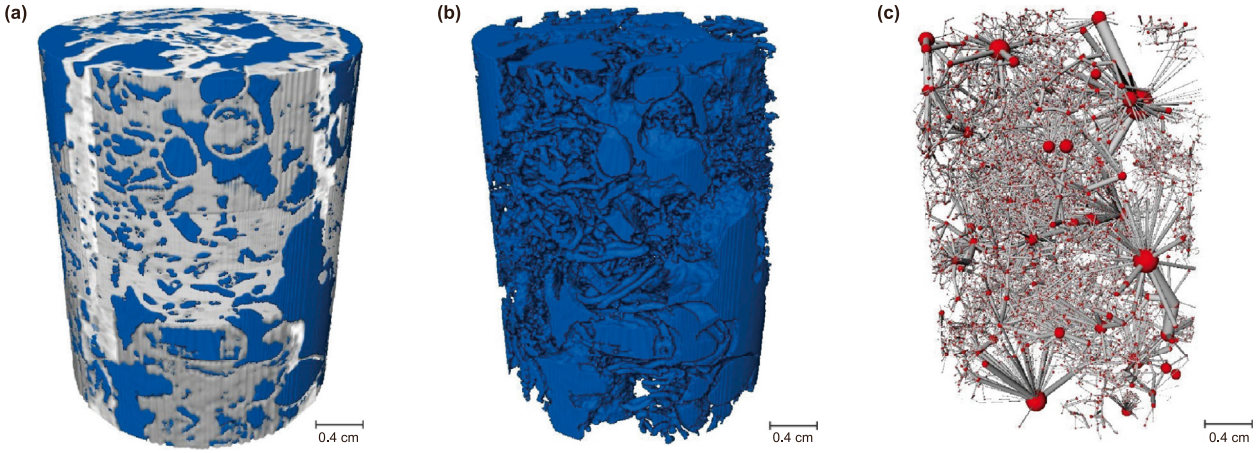

Fig. 8. 3D visualization of F1-1 columnar sample obtained from micro-CT scan images for (**a**) grain (gray) and total pores (blue), (**b**) connected pores (blue), and (**c**) pore network model.

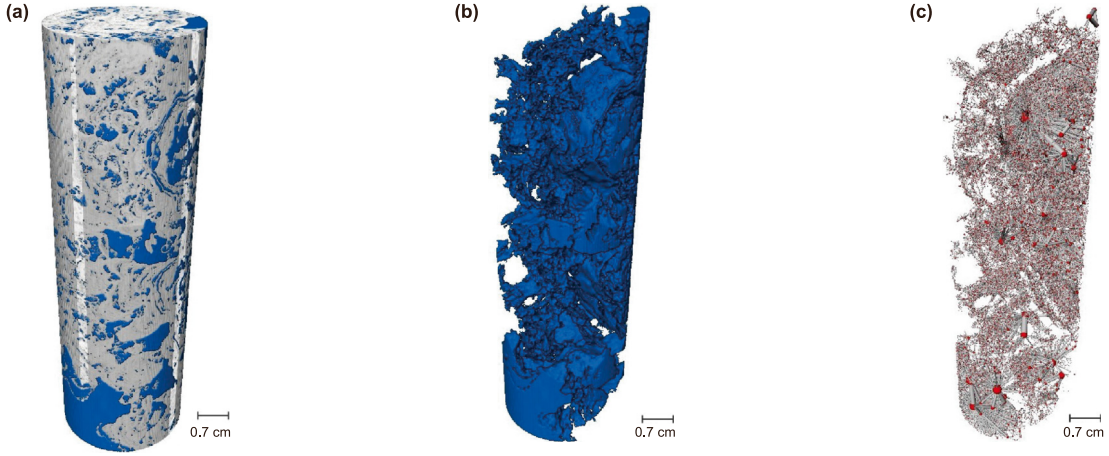

Fig. 9. 3D visualization of F2-6 fine-grained sample obtained from micro-CT scan images for (**a**) grain (gray) and total pores (blue), (**b**) connected pores (blue), and (**c**) pore network model.

and throat radius (Fig. 10(f)). Since most data for coordination number fell between one and 25, two plots were considered, one focusing on all the data in the log scale and the other on most of the data in the linear scale.

The medians of all the PNM properties are listed in Table 5. Samples from both facies displayed the same median coordination number of 3. However, compared to the fine-grained sample, the columnar sample exhibits substantially higher relative frequency for the coordination number of less than 3, but for higher coordination numbers, the fine-grained sample displayed more frequency (Fig. 10(a) and (b)), indicating improved pore connectivity. Additionally, the pore network in the fine-grained sample was composed of pores typically 86 μm in radius and throats 43 and 207 μm in radius and length, respectively. While median values of 142, 80, and 272 μm for pore radius, throat radius, and throat length, were measured for the network of the columnar sample. For the columnar sample, the pore network was generally comprised of larger, wider, and longer pores but with weaker connections and fewer junctions of throats to pores.

The shape factor refers to a unitless parameter used to quantify the degree of irregularity of a given geometric shape and represents a shape that matches the pore cross-section (Helland et al., 2008). It is defined as,

$$G = \frac{A}{S^2} \tag{3}$$

where A and S are the area and perimeter of the pore cross-section, respectively. If $G \leq \sqrt{3}/36$, then a triangle with the same G number is the idealized shape; if $\sqrt{3}/36 < G \leq 1/16$, then it is a square, and if $1/16 < G$, then it is a circle describing the pore cross-section (Helland et al., 2008).

Typically, the triangle represented the cross-section of pores from both facies. However, square pores were also available in both samples.

Fig. 11 displays the correlation between the cross-sectional area and volume of pores for both samples and compares them with sphere and tetrahedron pores. In fine-grained and columnar samples, for a given cross-section area, the volume of most pores is in the same range and greater in size than sphere and tetrahedron pores. Gaining a deeper understanding of the nature of pore space connectivity requires quantifying the correlation between the key pore geometry characteristics determined by pore network modeling. The relationships between important factors related to pores and throats are shown in Fig. 12(a) and (b): coordination number versus pore radius and Fig. 12(c) and (d): throat length versus throat radius. To provide a more detailed analysis of pore

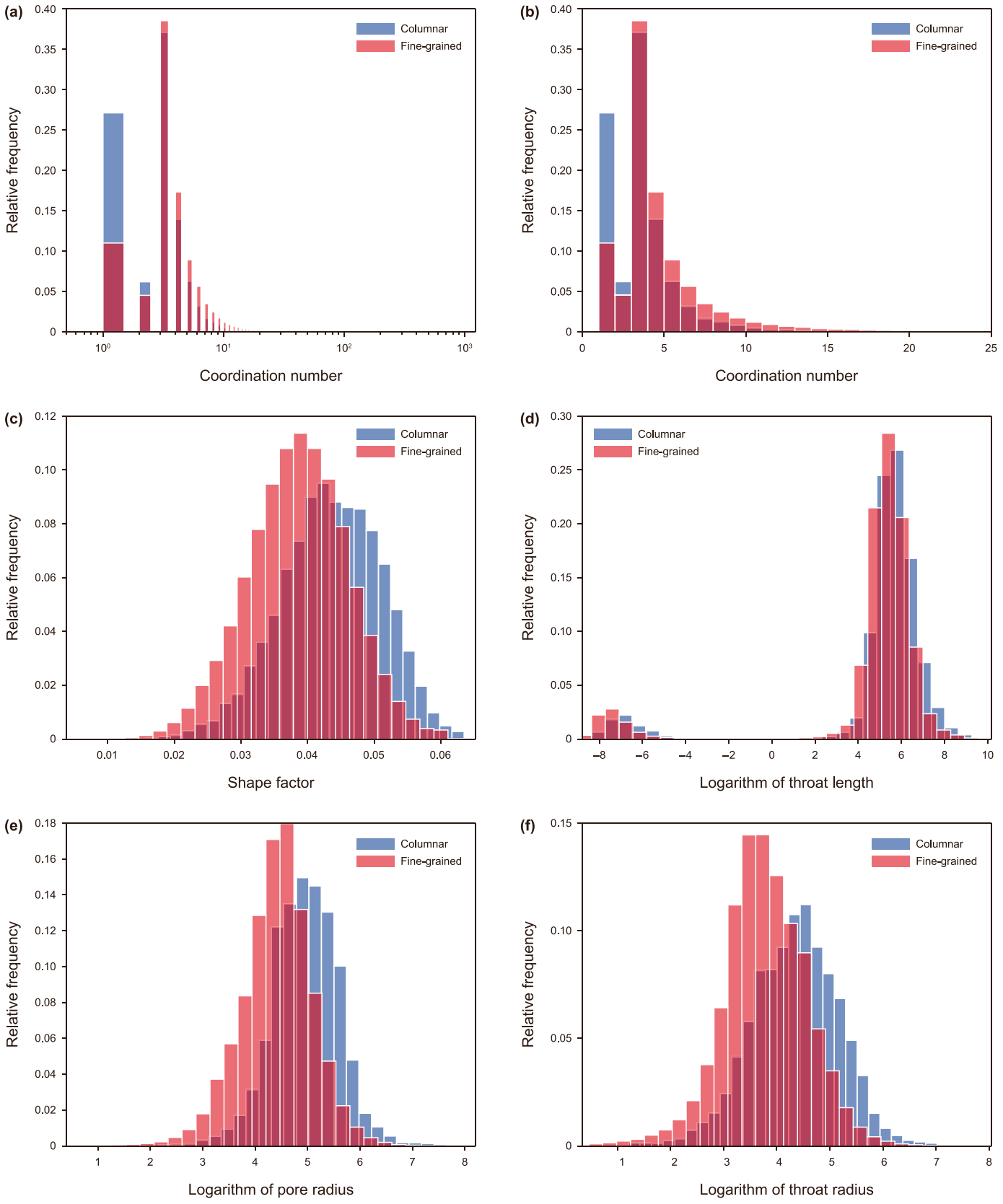

Fig. 10. Probability distribution graphs of PNM properties for columnar (blue) and fine-grained (red) samples for (**a**) coordination number in log scale for the entire data set, (**b**) coordination number in linear scale for the most frequent data set, (**c**) shape factor, (**d**) throat length, (**e**) pore radius, and (**f**) throat radius. The units of throat length, throat radius and pore radius are μm.

Table 5
Summary of the median of pore network characteristics of both facies.

Facies	Plug	Coordination number	Shape factor	Pore radius, μm	Throat radius, μm	Throat length, μm	Pore cross section area, μm^2	Pore volume, μm^3	Number of pores	Number of throats
Fine-grained	F2-6	3	0.0387	86.029	43.09	207.446	39,790	9,996,530	90,790	207,354
Columnar	F1-1	3	0.0437	141.985	80.132	271.683	114,839	40,610,900	12,128	20,090

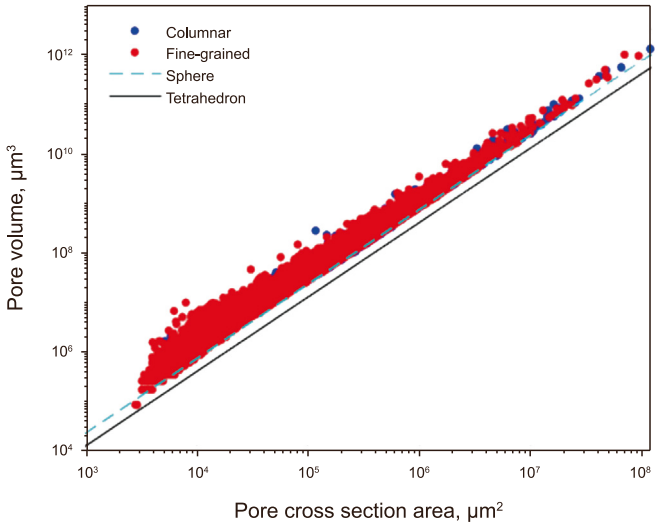

Fig. 11. The correlation between the pore area and pore volume columnar (blue) and fine-grained (red) samples.

and throat characteristics variations, Fig. 12(b) and (d) present coordination number versus pore radius and throat length versus throat radius, respectively. For these figures, the dataset was segmented into 500 μm intervals and the intermediate values within each interval were represented, while the standard deviation was plotted as error bars.

According to Fig. 12(a) and (b), the pore radius and coordination number are almost positively related to fine-grained samples, meaning that larger pores often connect to more throats. However, for the columnar sample, this relation was weaker. This means that different slopes can be observed for the two facies; in the fine-grained sample, as the pore radius rises, the coordination number is more considerable, while larger pores are less connected in the columnar sample. Fig. 12(c) and d reveal a more evident correlation between throat length and radius in both facies and depicts a significantly smaller variability in throat radius compared with variation in throat length. Compared to the columnar sample, there are few throats in the fine-grained sample that are longer and wider.

The variabilities of pore radius, throat radius, and throat length expressed through their respective coefficients of variation are additional pore geometry features that can be used to describe the PNM. The coefficient of variation is a unitless parameter that can be used as an all-encompassing description of pore geometry despite changes in porosity and mineral composition (Bernabé et al., 2010; Thomson et al., 2018). These results are listed in Table 6. The coefficient of variation greater than 1, indicates an unusually high standard deviation of the parameters, which is in good agreement with the high heterogeneity of our sample.

3.1.2. Porosity and 3D visualization from medical CT images

The porosity value for each 2D slice was calculated using the obtained medical CT images from dry and wet flooding experiments, and porosity curves were generated over the length of the samples. The curves are shown in Fig. 13 with the means of 0.524, 0.298, and 0.243 for F1-1, F2-5, and F2-6 plugs, with a higher profile for the columnar sample that reveals the existence of large-scale void spaces in this sample. Each of the three profiles exhibits diverse porosities that differ in magnitude throughout the lengths, with the porosity varies from 0.45 to 0.61, from 0.23 to 0.42, and from 0.16 to 0.33 for F1-1, F2-5, and F2-6 plugs.

Fig. 14 displays the 3D visualization model of the porous system for three samples. Blue segmentations show connected pores, and gray segmentations show disconnected pores. In these models, white (background color) segmentations indicate grains. The disconnected pores (gray segmentation) are more dominant in the columnar sample. There are many disconnected pores and dead-end pores in too many areas of the samples that would probably block the flow in that direction and cause non-continuity in flow patterns. Since fluid flow patterns in these 3D models were not easy to observe (red lines), the upcoming 3D flow patterns (next figures) were displayed in a 2D plane of the porous system for better visualization and analysis, which means that flow patterns were generated and displayed for all the pores in the 3D model, while the connected pore system (only blue segmentations) of one longitudinal cross-section of the plugs was displayed as a background.

3.2. Single-phase studies

The first step of the single-phase studies was the injection of the DW at an injection rate of 0.1 mL/min as a tracer into the plug saturated with FB in conjunction with CT scanning. The process was followed by the injection of FB at a constant injection rate of 0.5 mL/min and the conduction of CT scanning during the flooding. The CT image files were processed to generate flow patterns, and the signals were split into two parts to separate fluids and show the displaced and displacing fluid flowlines during injection processes.

The flow lines of DW (yellow lines) during displacement of FB by DW in the porous medium for the three samples are indicated in Fig. 15. As mentioned, the blue parts in these images indicate connected pores of one longitudinal cross-section of the plugs.

In the case of the columnar sample, flow lines are distributed in only some parts of the sample (Fig. 15(a)), and the upper left side of the plug practically lacks flow patterns. It implies that the heterogeneity and disconnected/dead-end pores significantly affect the flow patterns. However, there is a more homogenous distribution of flow lines and better dispersion of the fluid along the samples for fine-grained plugs (Fig. 15(b) and (c)) during this miscible process, indicating higher sweep efficiency.

To obtain further in-depth information on the single-phase studies, after the injection of DW, the process was followed by the injection of FB with a rate of 0.5 mL/min coupled with CT

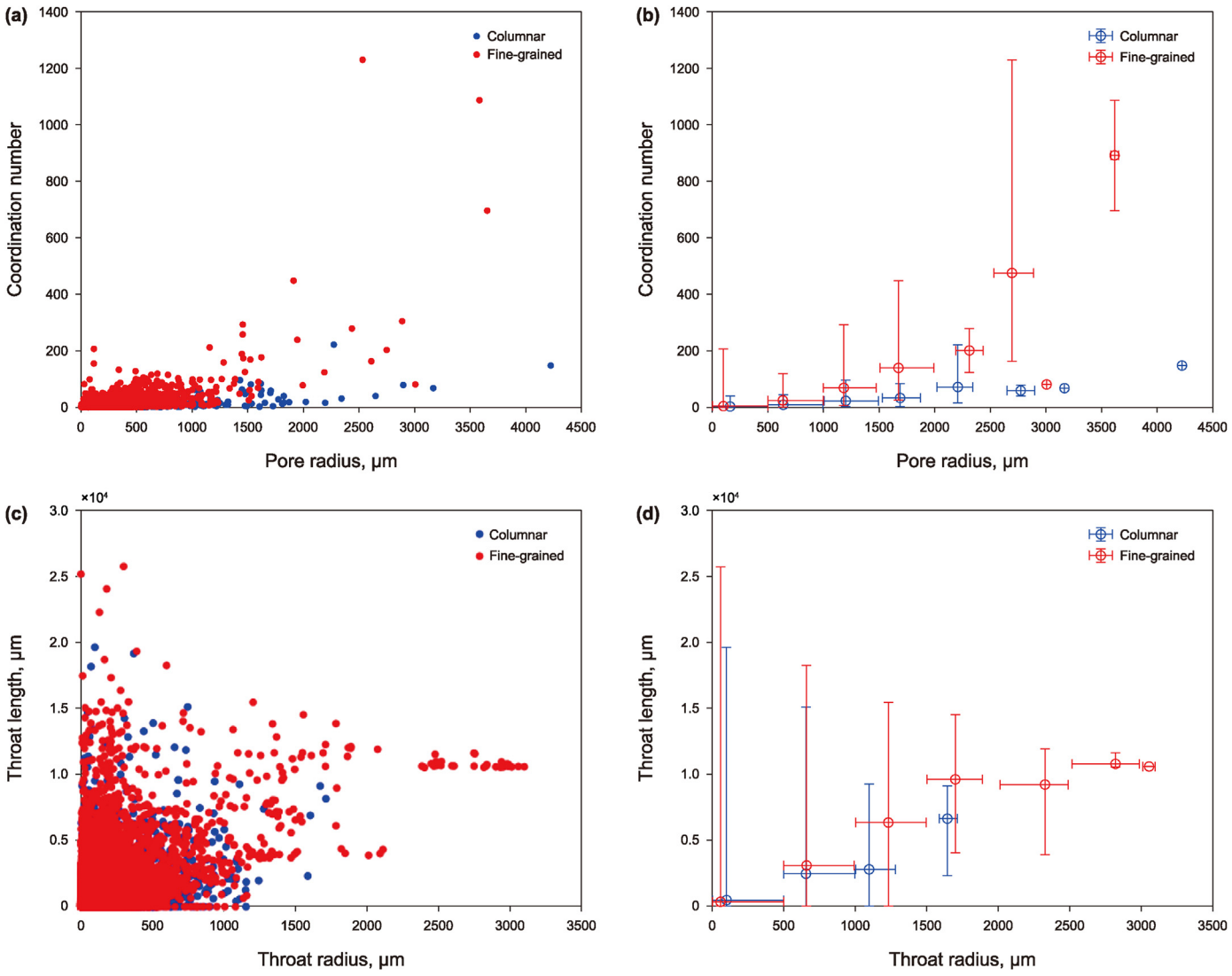

Fig. 12. The relationship between (**a**, **b**) coordination number and pore radius, (**c**, **d**) throat length and throat radius in columnar (blue) and fine-grained (red) samples.

Table 6
Coefficient of variation for pore radius, throat radius, and throat length for both facies sample.

Plug	Facies	$\sigma_r/\langle r\rangle$		$\sigma_l/\langle l\rangle$
		Pore	Throat	Throat
F2-6	Fine-grained	0.8369	1.1897	1.8045
F1-1	Columnar	0.8555	0.9491	1.7470

Notes: σ_r is the standard deviation for radius; σ_l is the standard deviation for length; $\langle r\rangle$ is the mean radius; $\langle l\rangle$ is the mean length.

scanning to see the effect of the high rate on the flow patterns. The flow lines of FB (red lines) during this miscible displacement for the three samples are shown in Fig. 16.

By analyzing the flow lines of FB in Fig. 16(a), we can see the poor distribution of flow lines in the columnar sample, indicating unswept areas. During this high-rate miscible fluid transportation, F2-5 revealed significantly better fluid dispersion in comparison with F2-6 (Fig. 16(b) and (c)), which has a good agreement with the high amount of connected pores and their homogenous distribution in this sample (blue parts in Fig. 14(b)).

To conclude the single-phase step and prepare the sample for two-phase studies (preparation of fully FB-saturated plug), the injection rate for FB decreased to 0.1 mL/min until the total removal of the DW, and then FB was injected at different flow rates to validate the application of the Darcy law. Fig. 17 displays the example of the result of experiments for analyzing flow regimes in a vugular and a fine-grained plug. For all three samples, the dominant flow regime was Darcy, and no deviation from the straight line was observed in the plot of differential pressure over length versus velocity.

3.3. Two-phase studies

3.3.1. Oil injection (oil drainage)

In this step, the oil was injected (to achieve initial water saturation) at the rate of 0.1 mL/min into the samples in order to gain a clearer comprehension of the immiscible process and two-phase flow. Again, flow lines for this injection process were generated

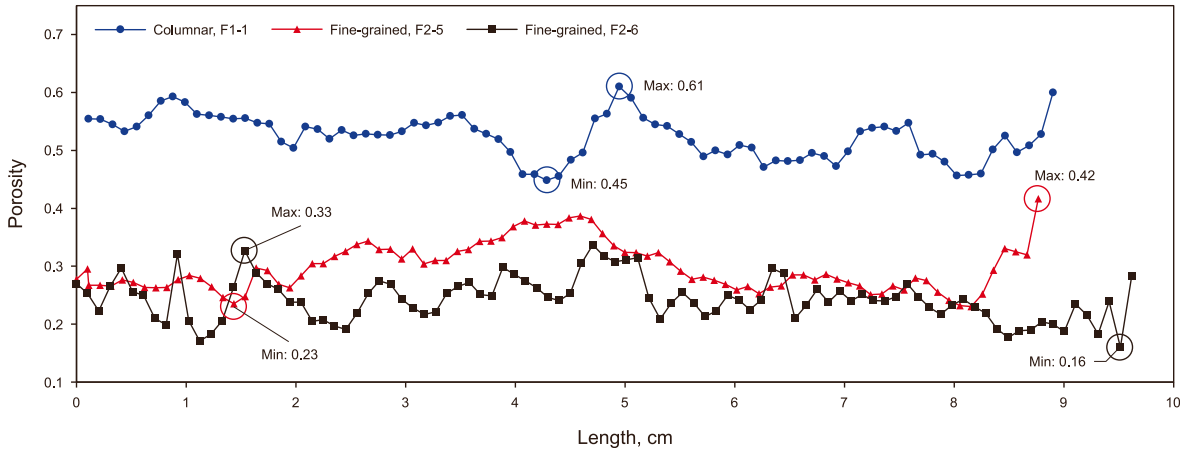

Fig. 13. Porosity distribution for the samples.

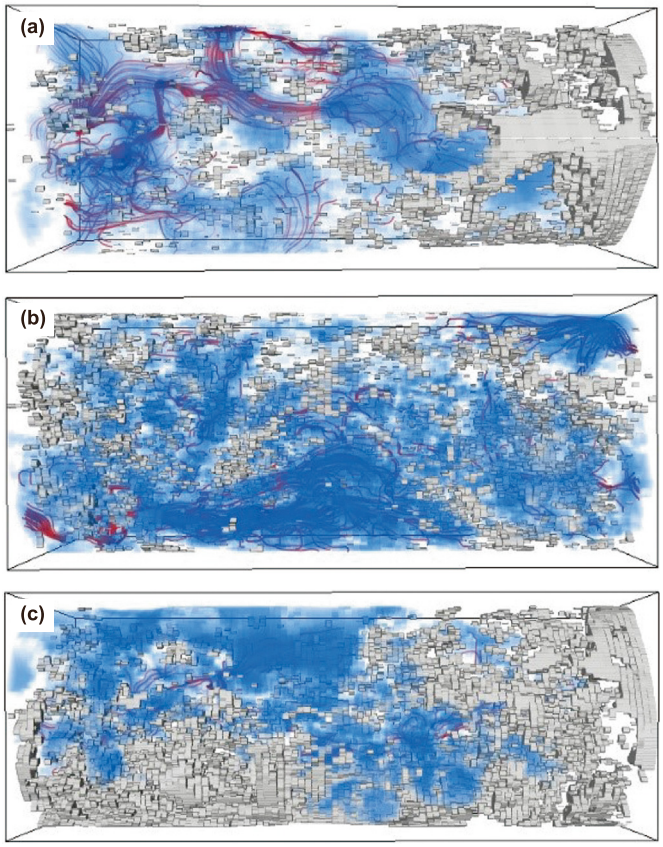

Fig. 14. Porous system for (**a**) F1-1 columnar plug, (**b**) F2-5 fine-grained plug, and (**c**) F2-6 fine-grained plug.

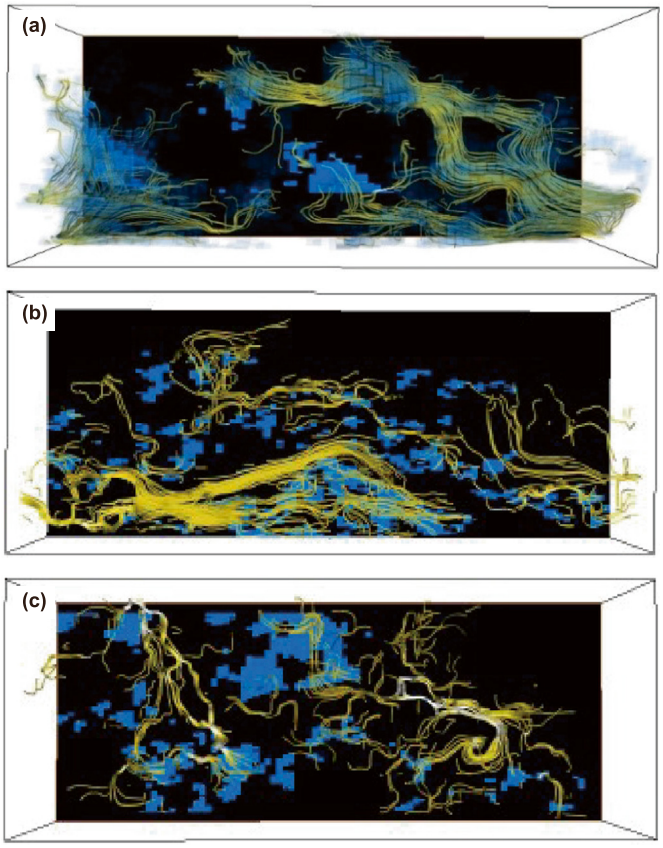

Fig. 15. Flow lines of DW (yellow lines) during flooding of DW and displacement of FB for (**a**) F1-1 columnar plug, (**b**) F2-5 fine-grained plug, and (**c**) F2-6 fine-grained plug.

by processing the CT image data. Like the previous section the flow paths and the behavior of fluid during transportation were analyzed. The flow lines of oil (displacing fluid: yellow lines) during displacement of FB in the porous system for the three samples are displayed in Fig. 18.

The oil flow pattern for all samples revealed a preferential displacement and mainly swept FB in some plug regions and bypassed it in other parts. The oil flooding yielded a relatively heterogeneous reduction of FB saturation, which can be seen from the number of flow lines in different plug regions. Some spaces without any flow lines indicate that oil was not imbibed into those FB-saturated parts of the porous network. However, we can see many oil flow lines covering most of the pore system in other parts.

The same results representing bypassing FB in the plug were

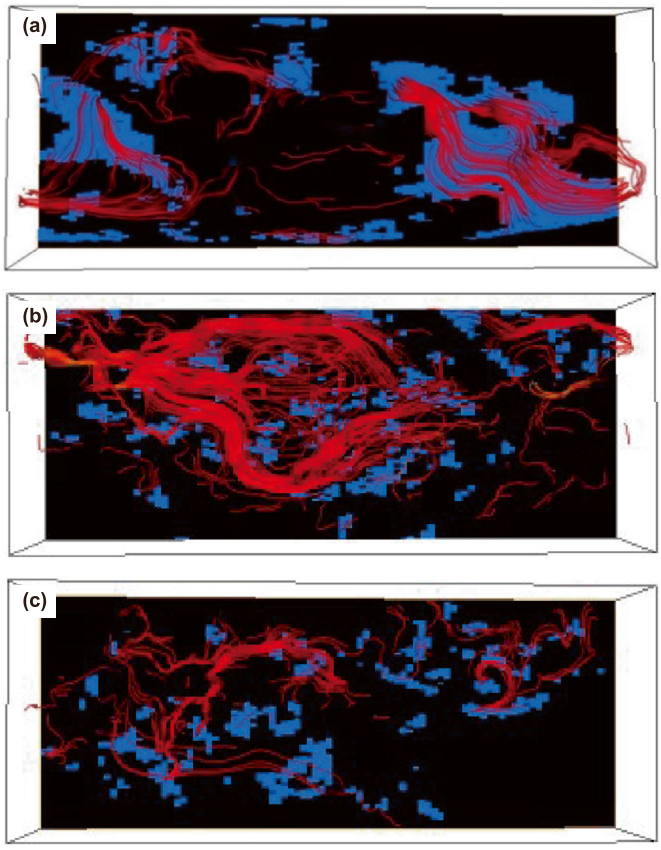

Fig. 16. Flow lines of FB (red lines) during injection of FB and displacement of DW for (**a**) F1-1 columnar plug, (**b**) F2-5 fine-grained plug, and (**c**) F2-6 fine-grained plug.

observed by analyzing the production data, including the amounts of oil and water volumes produced during tests. For the columnar sample, the total amount of produced water during oil flooding was approximately 32 cm^3 (the pore volume was 49.70 cm^3) representing the connate water saturation of 0.356. Table 7 (oil drainage columns) provides the results for the three samples.

Although the number of flow lines is more considerable in the columnar sample than in the fine-grained samples, it resulted in lower initial oil saturation at the final step of the oil flooding process (Table 7). This could be due to the large pore volume (around 50 cm^3) of this sample given the existence of large pores, which cause more streamlines of fluid in this process, but still, there are areas that remained untouched during this flooding process.

Throughout both the oil and FB injection experiments (next section), the alterations in the level of oil saturation in the plugs were regularly monitored and analyzed over time by utilizing medical CT imaging throughout the tests (Eq. (2)). The correlations between the amount of oil injection and oil saturation values versus length for the columnar plug and one fine-grained plug are shown in Fig. 19. The two oil saturation curves in the graphs correspond to the initial and final steps of oil flooding experiments.

According to Fig. 19, the following observations can be made.

- All curves clearly show variability in oil saturation value over the length. In the case of the columnar sample, the saturation varies between 0.02 and 0.25 at the initial step of oil flooding and between 0.52 and 0.97 at the final step of flooding. In the fine-grained sample, the values ranged from 0.002 to 0.22 and from 0.49 to 1 at two stages of flooding.
- As the oil saturation level increased, the spatial differences in the oil saturation values became increasingly noticeable.
- Oil breakthrough was observed shortly after the beginning of injection, and the level of oil saturation in both samples reached around 0.1 in the final layer (end of plugs) after 0.2 PV oil injection.
- Featuring the lowest point at around the midpoint of the core length, the oil saturation curves (for the two steps of the experiments) of the columnar sample displayed a strong

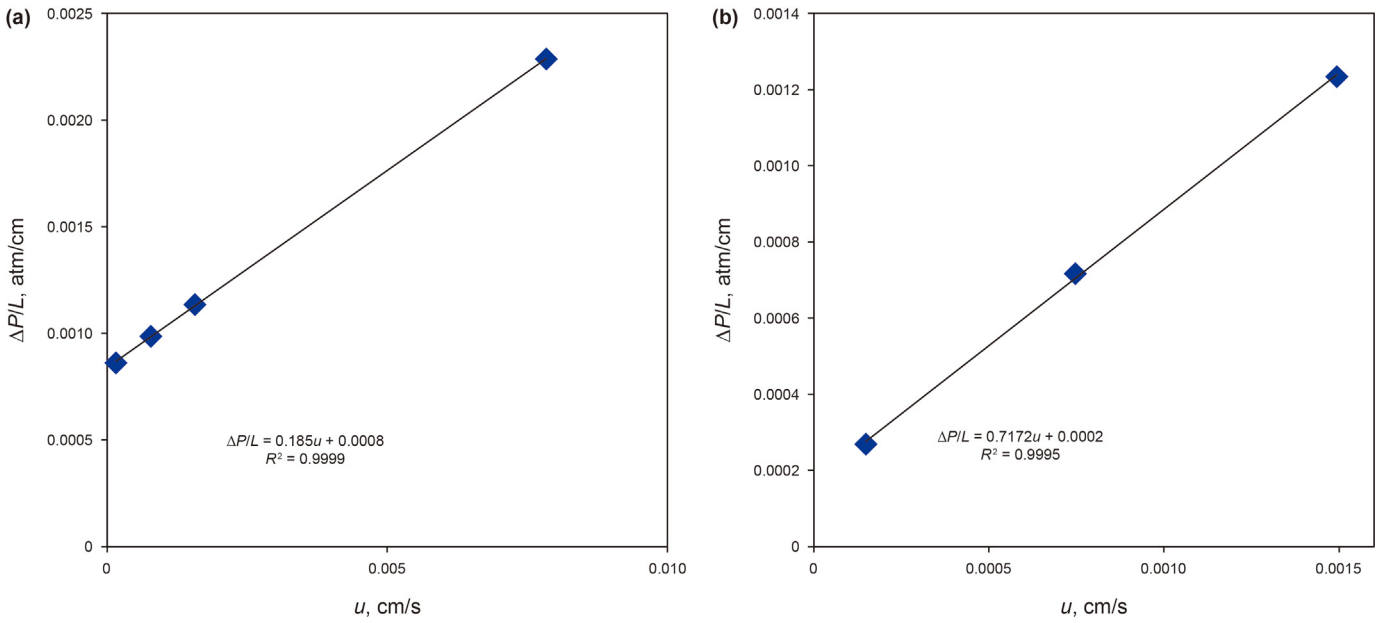

Fig. 17. Analyzing flow regimes for (**a**) F1-1 columnar plug and (**b**) F2-6 fine-grained plug. ΔP is the differential pressure, atm; L is the core length, cm; u is the velocity, cm/s.

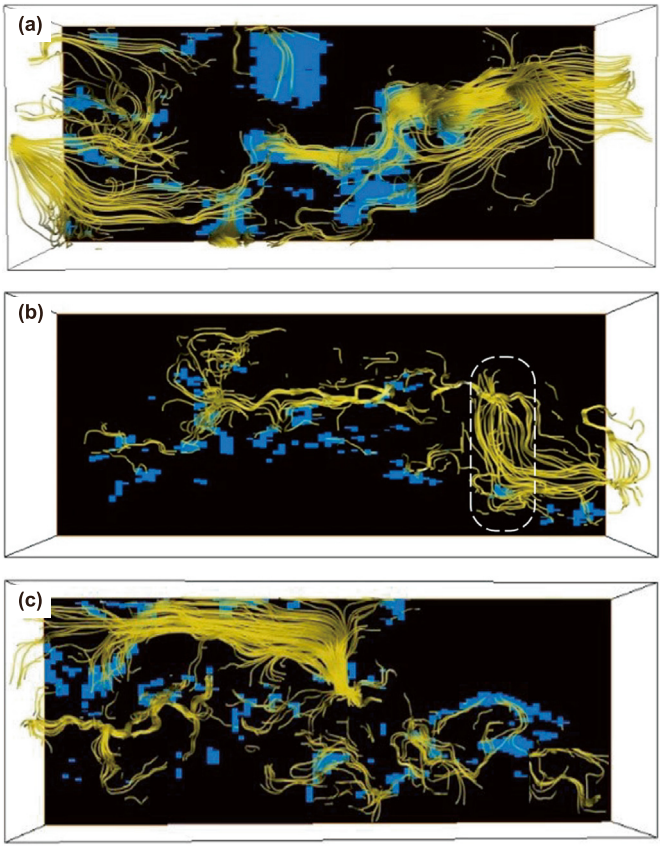

Fig. 18. Flow lines of oil (yellow lines) during flooding of oil and displacement of FB for (**a**) F1-1 columnar plug, (**b**) F2-5 fine-grained plug (white elliptic displays the area with an increase in the number of oil flow lines), and (**c**) F2-6 fine-grained plug.

correlation with the average porosity curve (Fig. 13). This can also be observed by the reduced number of flow lines in the middle of the sample (Fig. 18(a)).

- For the fine-grained sample, at the end of the injection, a peak with an oil saturation of one was observed at around one-third of the end of the plug; at the same area, we can see an increase in the number of oil flow lines (marked white area in Fig. 18(b)).
- For both samples, compared to the initial oil saturation profile (0.2 PV oil-injected), a shift in the shape of the profiles (believed to be caused by the selection of different preferential paths during the flow transfer) was noted at the end of the drainage experiment (2 PV oil-injected). However, this change is more considerable for the fine-grained sample.
- Mean oil saturation at the final step of oil flooding, 0.71 for the F1-1 columnar sample and 0.68 for the F2-5 fine-grained plug represents initial oil saturation (equivalent to 0.29 and 0.32 connate water saturation). By analyzing the data of core flooding tests, the same results were calculated (S_{wc} and S_{oi} in Table 7) and show acceptable concurrence with the saturation information acquired from CT measurements.

3.3.2. FB injection (water imbibition)

After the oil injection and reaching initial water saturation, FB was injected at a flow rate of 0.1 mL/min in conjunction with CT imaging to investigate the oil production process and to derive flow lines and saturation map for this two-phase immiscible process. Like the previous sections, the fluid flow paths and behavior during transportation were analyzed. The flow lines of oil (displaced fluid: yellow lines) during displacement of oil (FB imbibition) in the porous system for the three samples are displayed in Fig. 20.

The oil flow patterns of three samples showed preferential displacement, particularly sweeping oil in some parts and bypassing it in others. The number of flow lines in various plug locations indicates that the FB flooding resulted in a rather diverse drop in oil saturation. While there are many spaces without any particular flow lines, we can see a significant number of oil flow lines that cover nearly the whole region of the pore system in other parts, indicating that FB was imbibed better into those parts of the porous network. This indicates that we could not produce a significant portion of the oil due to the heterogeneity in the plugs. Core flooding results for this step showed 0.42, 0.49, and 0.571 residual oil saturation after FB injection for the F1-1, F2-5, and F2-6 plugs (Table 7).

The samples were CT-scanned periodically throughout the FB injection test to track the oil saturation level within the plugs, and the resulting saturation curves are displayed in Fig. 21 for the columnar and fine-grained samples. These two oil saturation curves correspond to the initial and final steps of FB flooding experiments.

The following findings can be drawn from Fig. 21.

- The change in oil saturation level over the length is seen for both samples. During the final stage of the FB flooding, the oil saturation levels for the columnar sample were between 0.21 and 0.71. On the other hand, the curve for the fine-grained sample revealed more heterogeneity, which varied between 0.08 and 0.84.
- The variations between the two curves exhibit the quantity of oil production. It indicates that oil production was more noticeable from the portion of the plug that the differences between the two lines increased (for example, at the beginning and end of the plug length for the columnar sample).
- Based on the differences between the two curves in the columnar sample, a high quantity of oil was left behind at around 2, 4.5, 5.5, and 8 cm in length; these points also have lower porosity levels.

Table 7
The outcomes of core flooding experiments conducted on three plugs.

Facies	Plug	Pore volume, cm^3	OOIP, cm^3	S_{wc}	S_{oi}	S_{or}	
			Oil drainage			FB imbibition	SB imbibition
Fine-grained	F2-5	29.76	21.0	0.294	0.706	0.487	0.487
	F2-6	26.26	21.0	0.200	0.800	0.571	0.571
Columnar	F1-1	49.70	32.0	0.356	0.644	0.422	0.392

Notes: OOIP: Original oil in place; S_{wc}: Connate water saturation; S_{oi}: Initial oil saturation; S_{oi}: Residual oil saturation.

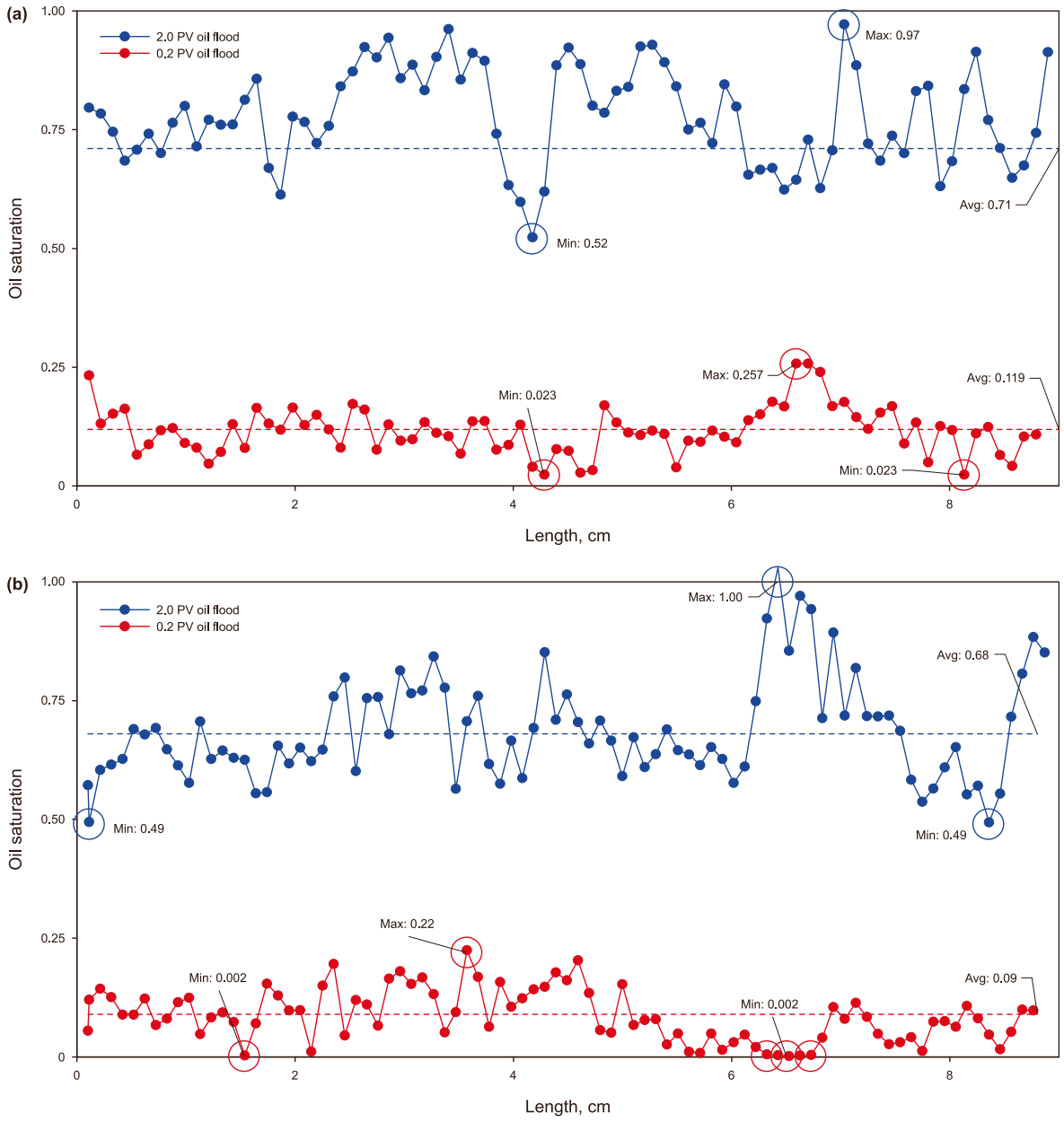

Fig. 19. Saturation curves for oil drainage stage for (**a**) F1-1 columnar plug and (**b**) F2-5 fine-grained plug.

- As was observed in the oil injection saturation results, the correlation between the saturation and the porosity curves was again evident.
- In the case of fine-grained samples, the oil saturation was decreased further on the upstream side than on the downstream side, and less variation was observed during FB flooding compared to oil flooding.
- In the last third of the fine-grained sample, it was observed that at some points, the oil saturation at the final step of the process (2 PV FB injection) was more than at the initial step (0 PV FB injection), it appears that oil has been pushed out from upstream areas and stacked here. The same results can be assessed in Fig. 20(b) where the increasing number of flow lines downstream of the plug can reveal oil accumulation.
- Compared to the initial oil saturation values (0 PV FB injection), a shift in the shape of the oil saturation profile (2 PV FB injection) was more noticeable for the fine-grained sample.
- In the case of the columnar sample, the oil flow lines during oil drainage (Fig. 18) and FB imbibition (Fig. 20) are distinct, and oil had selected various routes throughout these processes.
- Mean oil saturation at the end of FB injection (0.43 and 0.44 for the columnar and fine-grained sample, respectively), representing residual oil saturation of this process, have a respectable concurrence with the saturation data obtained from core flooding results (FB imbibition S_{or} in Table 7).

To conclude the two-phase step, SB was injected at a rate od 0.1 mL/min into plug samples, Fig. 22 indicates the recovery factor

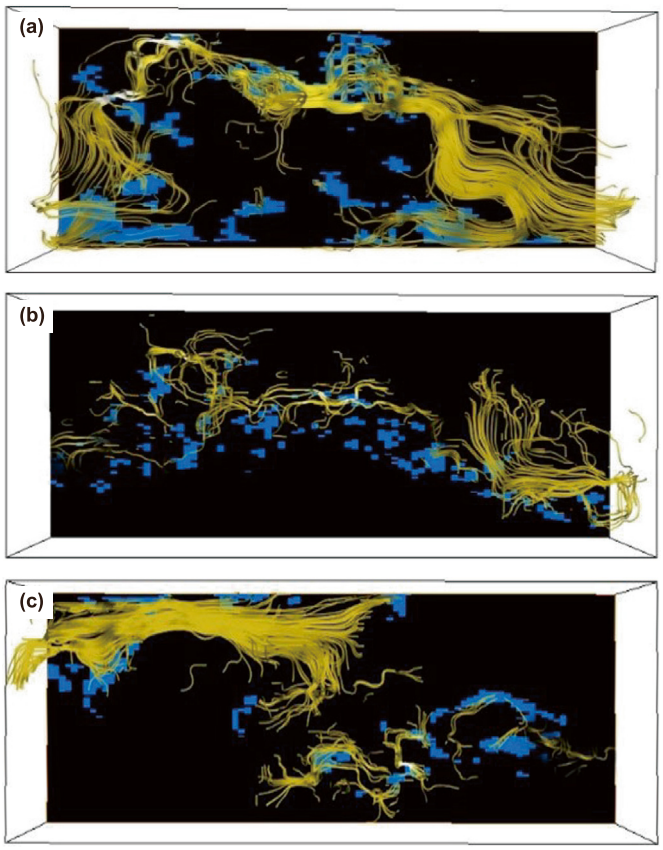

Fig. 20. Flow lines of oil (yellow lines) during injection of FB and displacement of oil for (**a**) F1-1 columnar plug, (**b**) F2-5 fine-grained plug, and (**c**) F2-6 fine-grained plug.

for FB flooding and subsequent SB injection. The recovery for fine-grained plugs remained practically unchanged with further SB injection. In contrast, the columnar sample demonstrated an additional 4.7% enhancement in oil recovery during this lower salinity water injection phase. This observed improvement in oil recovery in the columnar sample is now attributed to the potential influence of osmosis as one of the mechanisms contributing to enhanced oil recovery during low-salinity water injection. The proposed osmotic mechanism involves water transportation to large dead-end pores, facilitating oil mobilization within the porous media. It is crucial to note that while osmosis is suggested as one of the potential mechanisms, the complexity of reservoir conditions may involve a combination of factors influencing enhanced oil recovery during low-salinity water injection.

4. Conclusions

The primary objective of this investigation was to evaluate the impact of pore geometry, network characteristics, and heterogeneity on fluid flow through complex porous media. Three plugs were extracted from two distinct facies, namely fine-grained and vugular, which were identified based on the geological examination of the Lagoa Salgada outcrop samples to achieve this goal.

For the determination of the structure and geometry of the porous system, PNM was employed for the micro-CT images of samples from both facies to measure the connection between the features of the porous system, such as the radius of pore and throat, throat length, coordination number, shape factor, and the volume of pores. The median coordination number in samples from both facies was 3. Compared to the fine-grained sample, the less dense pore network of the columnar sample was typically comprised of larger pores and wider and longer throats but with a weaker connection of throats to pores (fine-grained: pores radius ~86 μm and throats radius ~43 μm, and columnar: pores radius ~142 μm and throats radius ~80 μm). For the fine-grained sample, the pore radius and coordination number showed an almost positive relation, meaning that pores with a greater size often linked to more channels, while in the columnar sample, larger pores were less connected. Both facies depicted significantly less variation in throat radius compared with throat length.

Medical CT imaging was employed in conjunction with core flooding experiments to comprehensively characterize the porous system, single-phase and two-phase flow patterns, and concentration profiles. Single-phase flow patterns suggested that the heterogeneity and disconnected/dead-end pores significantly affect the flow patterns. There was a more homogenous distribution of flow lines and better fluid dispersion along the samples with better pore network connectivity (fine-grained sample).

Two-phase flow patterns (drainage and imbibition) for all samples revealed a preferential and heterogeneous displacement that mainly swept displaced fluid in some regions of plugs and bypassed it in other parts. There were some pore spaces without any specific flow lines. At the same time, in other areas, a sizable number of flow lines completely covered the pore system, indicating that displacing fluid was more effectively imbibed into those parts of the porous network. The CT data identified oil saturation levels throughout the flooding stages, exhibiting diverse and non-homogenous values. The mean connate water and residual oil saturations ascertained from CT data at the final step of the oil and water flooding process exhibited a satisfactory concurrence with the saturation values derived from the amount of produced oil and brine. The heterogeneity of the sample significantly affects the flow patterns and saturation, and the correlation among the saturation and porosity distributions and the number of fluid flow patterns for the samples was evident. An alteration in the shape of the saturation curves was observed during the oil and water flooding, resulting from the selection of diverse pathways over time. This change was more prominent in the fine-grained sample.

Only for the columnar plug sample was the enhancement in oil recovery after shifting to lower salinity water injection (SB) observed according to the osmosis mechanism, while for the fine-grained samples, the recovery remained practically unchanged with further SB injection.

Overall, the results of this study emphasize the importance of understanding the heterogeneity and pore size distribution of porous media for predicting fluid propagation and fluid saturation in subsurface systems. These findings have implications for various applications, including oil and gas recovery, carbon capture and storage, and groundwater management.

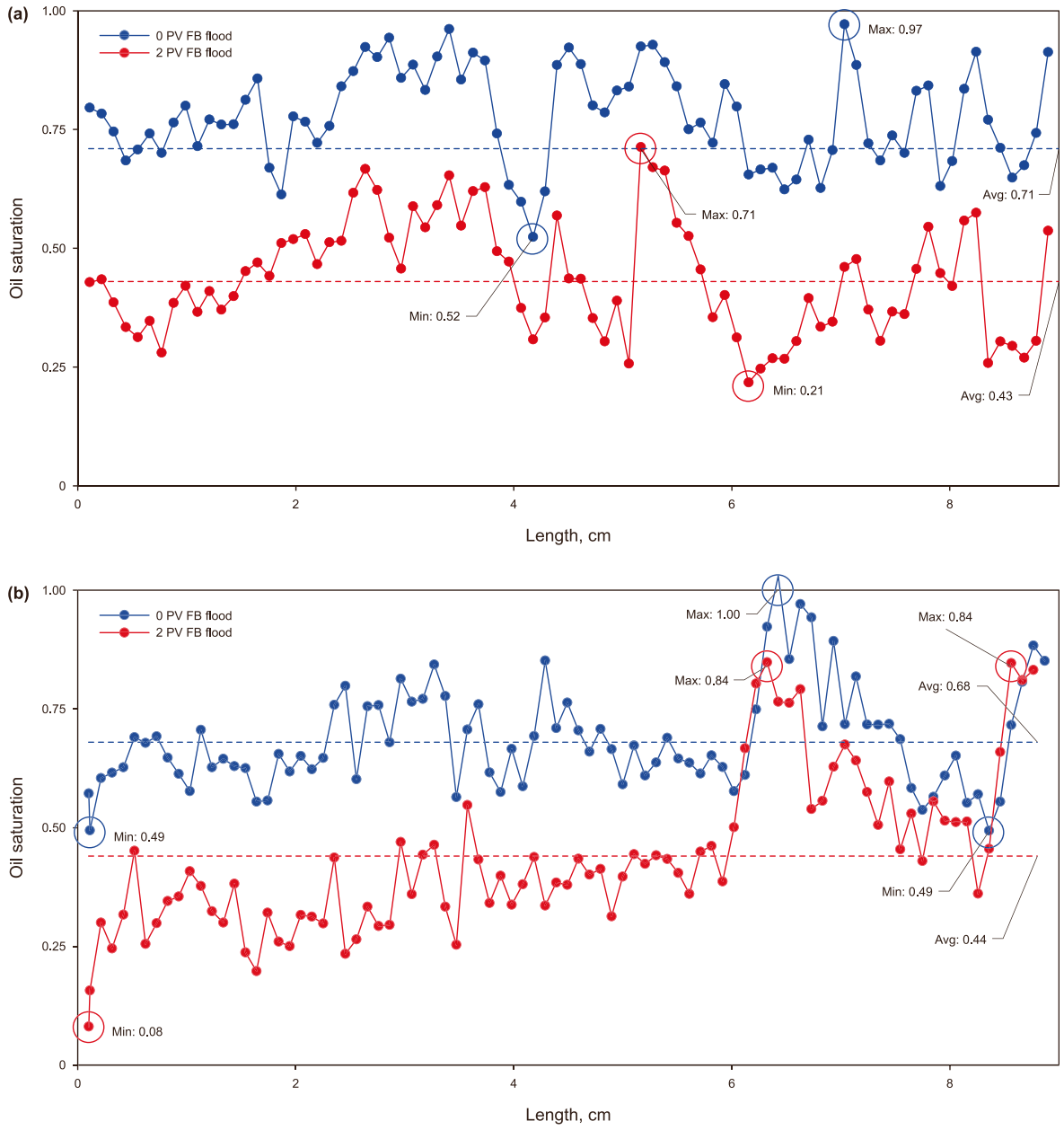

Fig. 21. Saturation curves for FB imbibition stage for (**a**) F1-1 columnar plug and (**b**) F2-5 fine-grained plug.

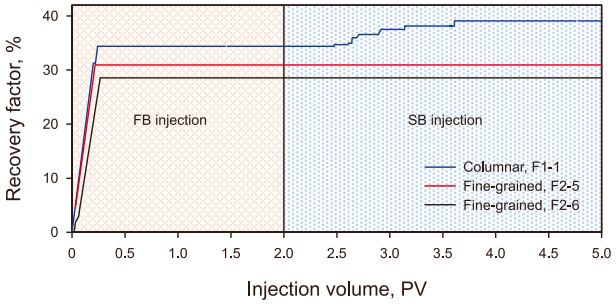

Fig. 22. The results of oil recovery factor for FB and SB flooding.

CRediT authorship contribution statement

Shohreh Iraji: Writing – original draft, Visualization, Software, Methodology, Investigation. **Tales Rodrigues De Almeida:** Visualization, Software, Methodology. **Eddy Ruidiaz Munoz:** Supervision, Methodology. **Mateus Basso:** Writing – review & editing, Supervision. **Alexandre Campane Vidal:** Writing – review & editing, Validation, Supervision, Project administration.

Declaration of competing interest

The authors declare that they have no known competing

financial interests or personal relationships that could have appeared to influence the work reported in this paper.

Acknowledgments

We gratefully acknowledge the support of EPIC – Energy Production Innovation Center, hosted by the University of Campinas (UNICAMP) and sponsored by FAPESP – São Paulo Research Foundation (2017/15736–3 process). We acknowledge the support and funding from Equinor Brazil and the support of ANP (Brazil's National Oil, Natural Gas and Biofuels Agency) through the R&D levy regulation. Acknowledgments are extended to the Center of Energy and Petroleum Studies (CEPETRO) and the School of Mechanical Engineering (FEM). We also thank PerGeos Software for licenses and technical support.

References

Abedi, B., Castaño, E.P.M., Heidaryan, E., Shadloo, M.S., 2020. Pore-scale visualization on polymer flooding: application of singular value decomposition-based image analysis method. J. Porous Media 23 (6). https://doi.org/10.1615/JPorMedia.2020033831.

Al-Kharusi, A.S., Blunt, M.J., 2007. Network extraction from sandstone and carbonate pore space images. J. Petrol. Sci. Eng. 56 (4), 219–231. https://doi.org/10.1016/j.petrol.2006.09.003.

Anbari, A., Chien, H.-T., Datta, S.S., et al., 2018. Microfluidic model porous media: fabrication and applications. Small 14 (18), 1703575. https://doi.org/10.1002/smll.201703575.

ASTM-D664, 2011. Standard Test Method for Acid Number of Petroleum Products by Potentiometric Titration-ASTM D 664-11A. ASTM International, West Conshohocken, PA. https://doi.org/10.1520/MNL10848M.

ASTM-D1298-12b, 2017. Standard Test Method for Density, Relative Density, or API Gravity of Crude Petroleum and Liquid Petroleum Products by Hydrometer Method. ASTM International West, Conshohocken, PA, USA. https://doi.org/10.1520/D1298-12BR17.

ASTM-D1744, 1992. Standard Test Method for Determination of Water in Liquid Petroleum Products by Karl Fischer Reagent. Annual Book of Standards.

ASTM-D2503-92, 1992. Standard Test Method for Relative Molecular Mass (Molecular Weight) of Hydrocarbons by Thermoelectric Measurement of Vapor Pressure. Annual Book of Standards.

ASTM-D6560-12, 2012. Standard Test Method for Determination of Asphaltenes (Heptane Insolubles) in Crude Petroleum and Petroleum Products. https://doi.org/10.1520/D6560-17.

ASTM-D7042, 2014. Standard Test Method for Dynamic Viscosity and Density of Liquids by Stabinger Viscometer (And the Calculation of Kinematic Viscosity). ASTM International.

Bernabé, Y., Li, M., Maineult, A., 2010. Permeability and pore connectivity: a new model based on network simulations. J. Geophys. Res. Solid Earth 115 (B10). https://doi.org/10.1029/2010JB007444.

Bruhn, C.H., Pinto, A.C., Johann, P.R., et al., 2017. Campos and Santos basins: 40 years of reservoir characterization and management of shallow-to ultra-deep water, post-and pre-salt reservoirs-historical overview and future challenges. In: Offshore Technology Conference Brasil. https://doi.org/10.4043/28159-MS.

Claes, H., Erthal, M.M., Soete, J., et al., 2017. Shrub and pore type classification: petrography of travertine shrubs from the Ballık-Belevi area (Denizli, SW Turkey). Quat. Int. 437, 147–163. https://doi.org/10.1016/j.quaint.2016.11.002.

Doyen, P.M., 1988. Permeability, conductivity, and pore geometry of sandstone. J. Geophys. Res. Solid Earth 93 (B7), 7729–7740. https://doi.org/10.1029/JB093iB07p07729.

Fetter, C.W., 2018. Applied Hydrogeology. Waveland Press.

Gunde, A.C., Bera, B., Mitra, S.K., 2010. Investigation of water and CO_2 (carbon dioxide) flooding using micro-CT (micro-computed tomography) images of Berea sandstone core using finite element simulations. Energy 35 (12), 5209–5216. https://doi.org/10.1016/j.energy.2010.07.045.

Helland, J., Ryazanov, A., van Dijke, M.I.J., 2008. Characterization of pore shapes for pore network models. In: Proceedings of the 11th European Conference on the Mathematics of Oil Recovery (ECMOR XI), Bergen, Norway, pp. 8–11. https://doi.org/10.3997/2214-4609.20146420.

Hendry, J., Burgess, P., Hunt, D., Janson, X., Zampetti, V., 2021. Seismic characterization of carbonate platforms and reservoirs: an introduction and review. Geological Society, London, Special Publications 509 (1), 1–28. https://doi.org/10.1144/SP509-2021-51.

Hounsfield, G.N., 1973. Computerized transverse axial scanning (tomography): Part 1. Description of system. Br. J. Radiol. 46 (552), 1016–1022. https://doi.org/10.1259/0007-1285-46-552-1016.

Iassonov, P., Gebrenegus, T., Tuller, M., 2009. Segmentation of X-ray computed tomography images of porous materials: a crucial step for characterization and quantitative analysis of pore structures. Water Resour. Res. 45 (9). https://doi.org/10.1029/2009WR008087.

Iraji, B., Shadizadeh, S.R., Riazi, M., 2015. Experimental investigation of CO_2 huff and puff in a matrix-fracture system. Fuel 158, 105–112. https://doi.org/10.1016/j.fuel.2015.04.069.

Iraji, S., Ayatollahi, S., 2019. Experimental investigation on asphaltene biodegradability using microorganism: cell surface properties' approach. J. Pet. Explor. Prod. Technol. 9 (2), 1413–1422. https://doi.org/10.1007/s13202-018-0537-1.

Iraji, S., Soltanmohammadi, R., De Almeida, T.R., et al., 2022a. Laboratory and numerical examination of oil recovery in Brazilian Pre-salt analogues based on CT images. In: Third EAGE Conference on Pre Salt Reservoirs. https://doi.org/10.3997/2214-4609.202288005.

Iraji, S., Soltanmohammadi, R., Munoz, E.R., et al., 2022b. Experimental investigation of waterflooding performance by increasing copper ions in Brazilian Pre-Salt Rock. In: 83rd EAGE Annual Conference & Exhibition. European Association of Geoscientists & Engineers, pp. 1–5. https://doi.org/10.3997/2214-4609.202210500.

Iraji, S., Soltanmohammadi, R., De Almeida, T.R., et al., 2022c. Experimental investigation of single-phase flow pattern in highly heterogeneous carbonates rocks. Rio Oil & Gas 2022. IBP, Rio de Janeiro | Brasil. https://doi.org/10.48072/2525-7579.rog.2022.024.

Iraji, S., Soltanmohammadi, R., Matheus, G.F., et al., 2023a. Application of unsupervised learning and deep learning for rock type prediction and petrophysical characterization using multi-scale data. Geoenergy Science and Engineering 230, 212241. https://doi.org/10.1016/j.geoen.2023.212241.

Iraji, S., Soltanmohammadi, R., Munoz, E.R., et al., 2023b. Core scale investigation of fluid flow in the heterogeneous porous media based on X-ray computed tomography images: upscaling and history matching approaches. Geoenergy Science and Engineering, 211716. https://doi.org/10.1016/j.geoen.2023.211716.

Jensen, J., Lake, L.W., Corbett, P.W., Goggin, D., 2000. Statistics for Petroleum Engineers and Geoscientists, second ed. Gulf Professional Publishing.

Knackstedt, M., Carnerup, A., Golab, A., et al., 2013. Petrophysical characterization of unconventional reservoir core at multiple scales. Petrophysics 54, 216–223.

Lamas, L., Ruidiaz, E., Vidal, A., 2019. Automated methodology for detecting border in ct-scan images of non-circular rock samples. Brazilian Journal of Petroleum and Gas 13 (4). https://doi.org/10.5419/bjpg2019-0023.

Lucia, F., 1983. Petrophysical parameters estimated from visual descriptions of carbonate rocks: a field classification of carbonate pore space. J. Petrol. Technol. 35 (3), 629–637. https://doi.org/10.2118/10073-PA.

Markussen, Ø., Dypvik, H., Hammer, E., et al., 2019. 3D characterization of porosity and authigenic cementation in Triassic conglomerates/arenites in the Edvard Grieg field using 3D micro-CT imaging. Mar. Petrol. Geol. 99, 265–281. https://doi.org/10.1016/j.marpetgeo.2018.10.015.

Matula, M., 1969. Engineering geologic investigations of rock heterogeneity. In: The 11th US Symposium on Rock Mechanics (USRMS). American Rock Mechanics Association.

PerGeos, S., 2019. Tutorials. ThermoFisher Scientific.

Raeini, A.Q., Blunt, M.J., Bijeljic, B., 2014. Direct simulations of two-phase flow on micro-CT images of porous media and upscaling of pore-scale forces. Adv. Water Resour. 74, 116–126. https://doi.org/10.1016/j.advwatres.2014.08.012.

Rahmat, A., Nasiri, H., Goodarzi, M., Heidaryan, E., 2020. Numerical investigation of anguilliform locomotion by the SPH method. Int. J. Numer. Methods Heat Fluid Flow 30 (1), 328–346. https://doi.org/10.1108/HFF-05-2019-0391.

Rezende, M.F., Tonietto, S.N., Pope, M.C., 2013. Three-dimensional pore connectivity evaluation in a Holocene and Jurassic microbialite buildup. AAPG (Am. Assoc. Pet. Geol.) Bull. 97 (11), 2085–2101. https://doi.org/10.1306/05141312171.

Sen, S., Abioui, M., Ganguli, S.S., et al., 2021. Petrophysical heterogeneity of the early Cretaceous Alamein dolomite reservoir from North Razzak oil field, Egypt integrating well logs, core measurements, and machine learning approach. Fuel 306, 121698. https://doi.org/10.1016/j.fuel.2021.121698.

Sharma, M., 2008. Stromatolites studies in India: an overview. Journal of Palaeosciences 57 (1–3), 63–67. https://doi.org/10.54991/jop.2008.228.

Soltanmohammadi, R., Iraji, S., De Almeida, T.R., et al., 2021. Insights into multiphase flow pattern characteristics and petrophysical properties in heterogeneous porous media. In: Second EAGE Conference on Pre-salt Reservoir. European Association of Geoscientists & Engineers, pp. 1–5. https://doi.org/10.3997/2214-4609.202183016.

Soltanmohammadi, R., Iraji, S., De Almeida, T.R., et al., 2022. Upscaling challenges of heterogeneous carbonate rocks: A case study of Brazilian pre-salt analogous. In: Third EAGE Conference on Pre Salt Reservoirs. https://doi.org/10.3997/2214-4609.202288013.

Soltanmohammadi, R., Iraji, S., De Almeida, T.R., et al., 2024. Investigation of pore geometry influence on fluid flow in heterogeneous porous media: a pore-scale study. Energy Geoscience 5 (1), 100222. https://doi.org/10.1016/j.engeos.2023.100222.

Su, H., Zhou, F., Zheng, A., et al., 2022. Heavy oil recovery by alkaline-cosolvent-

polymer flood: a multiscale research using micromodels and computed tomography imaging. SPE J. 27 (3), 1480–1492. https://doi.org/10.2118/204766-PA.

Thomson, P.-R., Aituar-Zhakupova, A., Hier-Majumder, S., 2018. Image segmentation and analysis of pore network geometry in two natural sandstones. Front. Earth Sci. 6, 58. https://doi.org/10.3389/feart.2018.00058.

Thomson, P.-R., Jefferd, M., Clark, B.L., et al., 2020. Pore network analysis of brae formation sandstone, North Sea. Mar. Petrol. Geol. 122, 104614. https://doi.org/10.1016/j.marpetgeo.2020.104614.

Vik, B., Bastesen, E., Skauge, A., 2013. Evaluation of representative elementary volume for a vuggy carbonate rock—part: Porosity, permeability, and dispersivity. J. Petrol. Sci. Eng. 112, 36–47. https://doi.org/10.1016/j.petrol.2013.03.029.

von Bargen, N., Waff, H.S., 1986. Permeabilities, interfacial areas and curvatures of partially molten systems: results of numerical computations of equilibrium microstructures. J. Geophys. Res. Solid Earth 91 (B9), 9261–9276. https://doi.org/10.1029/JB091iB09p09261.

Wimert, J., Hier-Majumder, S., 2012. A three-dimensional microgeodynamic model of melt geometry in the Earth's deep interior. J. Geophys. Res. Solid Earth 117 (B4). https://doi.org/10.1029/2011JB009012.

Withers, P.J., Bouman, C., Carmignato, S., et al., 2021. X-ray computed tomography. Nature Reviews Methods Primers 1 (1), 1–21. https://doi.org/10.1038/s43586-021-00015-4.

Wright, P., Tosca, N., 2016. A Geochemical model for the formation of the pre-salt reservoirs, Santos Basin, Brazil: Implications for understanding reservoir distribution. AAPG Search and Discovery article, 51304.